



# Development of a novel direct powder screw extruder for 3D scaffold printing of PCL-based composites

Trung Kien Nguyen<sup>1</sup> · Bang Thi Le<sup>2</sup> · Minh Thi Hong Nguyen<sup>3</sup> · Van-Sang Pham<sup>1</sup> · Truong Do<sup>4</sup> · Phuong Tran<sup>5</sup> · Lan Xuan Phung<sup>1</sup>

Received: 24 January 2023 / Accepted: 29 July 2023 / Published online: 16 August 2023  
© The Author(s), under exclusive licence to Springer-Verlag London Ltd., part of Springer Nature 2023

## Abstract

Polycaprolactone (PCL) has emerged as a prominent biomaterial for fabricating scaffolds in tissue engineering applications via 3D printing. However, the common commercial form of PCL is typically observed in powder or pellets, which may not be conducive for deployment in traditional 3D fused deposition modeling (FDM) printers that utilize filaments. Moreover, most additive biomaterials that are mixed with PCL commonly exist in a powdered form. Consequently, the primary drawback of the conventional FDM printing method arises from the requirement to convert into a filament form. This research addresses the abovementioned constraint by developing and optimizing a novel design of a direct powder mini-screw extruder (DPSE) through numerical modeling analysis. The cost-effective DPSE printer head enables the printing of not only pure PCL but also PCL-based composite scaffolds by utilizing a combination of PCL powder and other biomaterials such as thermoplastic polymers, hydrogels, or ceramics. Microscopy, scanning electron microscopy (SEM), and attenuated total reflection Fourier-transform infrared (ATR-FTIR) spectroscopy are employed to characterize the morphology, surface roughness, and chemical composition of the porous scaffolds. Furthermore, other characteristics of the 3D PCL-based composite scaffolds, including wettability, mechanical properties, and cell attachment, are also investigated. The experimental study investigates the influence of printing parameters on the printed line width for each PCL-based composite. Through these investigations, this work demonstrates the high potential of the novel DPSE printer head in fabricating high-quality PCL-based composite scaffolds with minimal wastage and prolonged printability.

**Keywords** Scaffold · Tissue engineering · 3D printing · PCL-based composites · Screw-based extruder · Additive manufacturing

## 1 Introduction

Tissue engineering represents an emerging interdisciplinary field aimed at developing biological substitutes to restore, maintain, or enhance the functionality of damaged tissues. Within this context, scaffolds play a crucial role as temporary porous structures that mimic the extracellular matrix, facilitating cell proliferation and promoting tissue regeneration. The ideal scaffold holds a porous architecture with interconnected pores, enabling cell growth, oxygen supply, and nutrient diffusion [1]. Furthermore, the scaffold should exhibit biocompatibility and undergo biodegradation at a favorable rate for successful host tissue regeneration. It must possess appropriate mechanical properties and surface topography to support cell adhesion, proliferation, and differentiation. Various biomaterials, including natural and synthetic polymers, ceramics, metals, and composites, are

---

✉ Lan Xuan Phung  
lan.phungxuan@hust.edu.vn

<sup>1</sup> School of Mechanical Engineering, Hanoi University of Science and Technology, Hanoi 10000, Vietnam

<sup>2</sup> School of Materials Science and Engineering, Hanoi University of Science and Technology, Hanoi 10000, Vietnam

<sup>3</sup> Department of Life Sciences, University of Science and Technology of Hanoi, Vietnam Academy of Science and Technology, Hanoi 10000, Vietnam

<sup>4</sup> College of Engineering and Computer Science, VinUniversity, Hanoi 10000, Vietnam

<sup>5</sup> School of Engineering, RMIT University, Melbourne, Australia

employed for fabricating 3D scaffolds. Each biomaterial possesses distinct mechanical properties, biological characteristics, and fabrication capabilities [2].

To construct the 3D porous scaffold, conventional and 3D printing techniques are commonly applied. In comparison to conventional techniques such as salt leaching, gas foaming, or freeze drying, 3D printing techniques offer significant advantages for controlling scaffold structures with diverse geometries and properties for tissue engineering applications. Typical 3D printing techniques employed for scaffold fabrication include stereolithography (SLA), selective laser sintering (SLS), binder 3D printing, solution-based dispenser (SBD), and fused deposition modeling (FDM) [3]. SLA and SLS employ laser sources as part of their build processes. In SLA, a liquid resin is solidified through curing, whereas SLS uses a heat source from the laser to sinter powdered material. SLA has a limited range of available biocompatible materials, while SLS offers a broader range of thermoplastic biomaterials [4, 5]. SLA and SLS demonstrate superior printing accuracy in comparison with other techniques. Consequently, these techniques are often employed in the production of complex 3D porous structures, such as triply periodic minimal surfaces (TPMS) or gyroid structures [6, 7]. Similar to the SLS technique, the binder 3D printing technique works on the powder-bed fusion principle; however, it employs liquid binding agents instead of the laser sintering method. Although these techniques can fabricate the 3D porous scaffold directly from powdered materials, they are primarily suited for fabricating free-standing scaffolds or implants and may present challenges when incorporating other printer heads for multi-material printing. The large initial powder quantity required when using powder-bed fusion is another limitation of these methods. The solution-based dispenser technique is used as a bioprinting technique for constructing hydrogel-based scaffolds for tissue engineering applications. FDM-based techniques are extensively employed for fabricating thermoplastic polymer-based specimens due to their simplicity, cost-effectiveness, and compatibility with multi-materials or multi-printer heads [8]. As a result, these techniques find significant suitability in constructing thermoplastic-based biomaterial structures for biomedical and tissue engineering applications [9, 10].

### 1.1 PCL-based composites

Thermoplastics, including polylactic acid (PLA), poly(lactic-co-glycolic acid) (PLGA), poly( $\epsilon$ -caprolactone) (PCL), and polyethylene glycol (PEG), are commonly used biomaterials in FDM-based techniques. Among these thermoplastic biomaterials, PCL is one of the most popular synthetic polymers for fabricating high-quality 3D porous scaffolds due to its long-term biodegradability, good biocompatibility, high

mechanical characteristics, and easy processability [11]. Nevertheless, PCL exhibits poor characteristics such as high hydrophobicity, limited cell adhesion ability, and restricted bioactivity. Therefore, the blending of PCL with synthetic or natural polymers, as well as ceramic materials, has been explored as a strategy to achieve the desired scaffold properties for tissue engineering applications. By incorporating these additional materials, the limitations of PCL can be moderated, leading to improved biocompatibility, enhanced cell adhesion, and expanded bioactivity, ultimately enhancing the overall performance and functionality of the scaffolds [12].

PEG, as a thermoplastic biopolymer, has gained extensive utilization in the field of tissue engineering due to its remarkable hydrophilicity, biodegradability, and biocompatible properties [13]. However, its mechanical property is relatively low, prompting the blending of the thermoplastic biopolymer with PCL to obtain the combined benefits of both biomaterials [14, 15]. Natural polymers such as gelatin, chitosan, collagen, and sodium alginate (SA) exhibit the advantages of biocompatibility and bioactivity, tailored cell growth, and adhesion [16]. Among these natural polymers, SA has found widespread application in tissue engineering for cell delivery and cell-free support owing to its high biocompatibility, cost-effectiveness, and rapid gelation facilitated by calcium ions [17]. Nevertheless, the inherent limitations of SA, such as low mechanical properties, high biodegradation rate, and limited printability, hinder its widespread application. To overcome these limitations, the integration of PCL with SA has been explored to fabricate hybrid or composite scaffolds, aiming to enhance the scaffold characteristics relating to wettability, cell behaviors, and biological activities [18–21]. Bioceramic-based calcium phosphate (i.e., hydroxyapatite (HA) and  $\beta$ -tricalcium (TCP)), which has a chemical composition similar to the mineral part of a bone, is widely used for bone substitute due to good biocompatibility and bioactivity [22, 23]. Thus, the mixture of PCL/HA and PCL/TCP with different concentrations of bioceramic particles was investigated to develop bioactive polymer composite scaffolds [11, 24–27]. These combinations can yield a 3D composite scaffold with improved cell attachment, cell proliferation, and differentiation as ceramic components in the composite increase. The trend of combining various materials to fabricate 3D composite or hybrid scaffolds has gained popularity, enabling the exploitation of the tailored properties offered by each constituent material.

### 1.2 3D Printing techniques for composite scaffold fabrication

Fused deposition modeling (FDM) represents an extrusion technique that involves the melting and extrusion of

filaments or pellets through a nozzle to create a 3D object in a layer-by-layer fashion. The conventional approach to feeding filament (referred to as c-FDM) has demonstrated successful application in fabricating 3D scaffolds for hard-engineered tissue, such as bone and cartilage [26, 28]. However, the limited availability of commercial thermoplastic biomaterials or composites in filament form poses a significant drawback to the widespread adoption of c-FDM printers for tissue engineering applications. Even when specialized equipment is designed for filament production, the time-consuming process of filament formation contributes to a costly manufacturing process, thus serving as the primary obstacle to the utilization of c-FDM for biomaterials [29].

Consequently, numerous studies have focused on developing 3D scaffold printing techniques directly from raw materials in the form of pellets or powder. These alternative techniques include solution-based disperser (SBD), melt-based extrusion under pressure (m-FDM), and screw-based extrusion (s-FDM). SBD utilizes toxic solvents [25, 30], while m-FDM suffers from high waste generation and long-term thermal effects, leading to larger crystallite sizes, which negatively affect the biological performance of the printed scaffold [31, 32]. Although both methods are popular for fabricating composite scaffolds, they experience challenges in achieving high printing accuracy due to the reliance on pneumatic systems for material transfer and control, resulting in lower position accuracy compared to electric control systems. Moreover, the implementation of a compressed air system further adds complexity to the printing system, along with increased manufacturing and operational costs. Despite the challenges arising from its more complex design, s-FDM offers superior flow rate control compared to both previous techniques, owing to

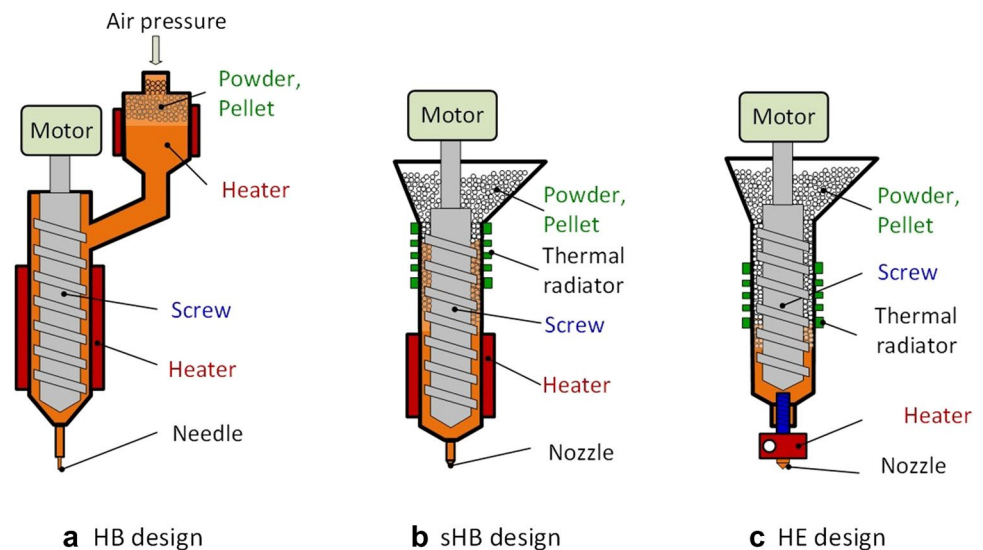
the rapid adjustment of screw speed rather than relying on air or piston pressure [32].

### 1.2.1 Screw-based extrusion

There are three common designs of s-FDM using a single screw, namely, hot barrel (HB), semi-hot barrel (sHB), and hot end (HE), as depicted in Fig. 1. The main differences among these designs are in the heater position and material supply method. The s-FDM technique based on the hot barrel (HB) design depicted in Fig. 1a incorporates a heated feeding material chamber and utilizes a pneumatic system to transfer the molten material to the heating screw barrel [33, 34]. The molten material within the barrel is subsequently extruded through the nozzle via a stepper motor integrated with the screw. Several studies utilized a commercially available HB-based system from 3D Discovery, RegenHU, Villaz-Saint-Pierre, Switzerland, for fabricating scaffolds comprising either a single material or composites [35, 36]. It demonstrated the effective achievement of high-accuracy printed lines and high-quality 3D scaffolds. However, high energy consumption, high material waste, and the complexity associated with compressed air constrained the system, representing major limitations.

In contrast, the semi-hot barrel (sHB) design illustrated in Fig. 1b uses an electrical heater positioned at the half end of the barrel without a separate heating chamber [37, 38]. In the case of a short screw in a system where heat is quickly transferred to the hopper, there is a risk of the material at the feed region melting, which can impede the flow of the feeding material. The sHB system employs a long screw driven by a stepper motor integrated with the coolant system to prevent heat propagation upward toward the hopper [39]. The hot end (HE) design depicted in Fig. 1c incorporates indirect heat transfer to the barrel via a heat block at the end,

**Fig. 1** Different designs of the screw-based extrusion printer head



similar to most conventional c-FDM 3D printers. However, this design exhibits significantly lower print quality due to unstable heat transfer and uneven powder melt extrusion compared to c-FDM [29]. To address this issue, Whyman et al. introduced a thermal barrier ring made of Teflon and a Glycol/water coolant system mounted on the top barrel to enhance thermal isolation in the upward direction [40]. Each design possesses specific advantages and limitations concerning manufacturing cost, printing quality, heat transfer control, and waste material generation.

This study proposes a modified s-FDM technique to enhance its advantages and address its inherent limitations. A comprehensive investigation is conducted, incorporating numerical modeling analysis and experimental printing tests, to evaluate the performance of a novel DPSE printer head. The numerical modeling analysis examines the thermal behavior inside the barrel and along the screw to identify an optimal design that minimizes waste material and enhances thermal stability. The cost-effective DPSE printer head is constructed without a specialized coolant system. Yet, it enables the fabrication of 3D scaffolds using a PCL-based composite material with the appropriate printing quality, minimal waste material generation, and high printability across various composite formulations. The flexible usage of the DPSE printer head is demonstrated not only for pure PCL material but also for PCL-based composites comprising synthetic thermoplastic polymers (PCL-PEG), natural polymers (PCL-SA), and ceramics (PCL-TCP). The production of pure PCL and PCL-based composite scaffolds using a DPSE printer head presents significant potential for scaffold fabrication. A comprehensive evaluation is conducted

to assess the effectiveness of PCL-based composite scaffolds for tissue engineering applications regarding printing accuracy, surface roughness, morphology, hydrophilicity, mechanical properties, and cell attachment of the printed composite scaffolds. These evaluations provide valuable insights into the performance and potential utility of PCL-based composite scaffolds constructed by the DPSE printer head in tissue engineering applications.

## 2 Printer head design and analysis using FEM

### 2.1 HE design-based printer head for PCL-based scaffold fabrication

Table 1 provides a comprehensive comparison of three different designs of screw-based extrusion (s-FDM) techniques. The HB design demonstrates several notable advantages. The homogeneous melt state of the materials along the screw inside the barrel ensures a stable extrusion rate, resulting in superior print quality compared to the other designs. It also offers excellent material flexibility for both pure thermoplastic polymers and composites. On the other hand, the sHB design does not exhibit any outstanding advantages and is, therefore, not recommended as a preferred option. In contrast, the HE design presents several merits, including reduced heating energy requirements for the printing process, minimized waste of dead material, cost-effectiveness, and low thermal effects. Moreover, it can be readily integrated into open-source FDM 3D printers, expanding

**Table 1** Characteristics of screw-based extrusion systems for scaffold fabrication

|                              | Hot barrel (HB)   | Semi-hot barrel (sHB)                   | Hot end (HE)                                     |
|------------------------------|---|---|--|
| Heater position              | Whole barrel  | Half barrel                             | End block  |
| Powder/Pellet supply         | Air pressure  | Gravity                                 | Gravity  |
| Waste material               | Large   | Medium                                  | Small  |
| Heat power                   | High  | Medium                                  | Small  |
| Cost                         | Expensive   | Medium                                  | Low  |
| Heat transfer control        | Easy  | Difficult                               | Medium   |
| Power                        | Electricity, air pressure   | Electricity                             | Electricity                                      |
| Speed                        | 1–10 mm/s <sup>(1)</sup> (pure PCL)<br>15–20 mm/s <sup>(2)</sup> (pure PCL) | 12–20 mm/s (pure PCL)                   | 10–12 mm/s (pure PLA)<br><i>Not used for PCL</i> |
| Material flexibility         | High  | Low                                     | Low  |
| Tolerance printed line width | ≤ 5% (pure PCL)   | 5–10% (pure PCL)                        | <i>Not used for PCL, low quality with others</i> |
| Material                     | PLA, PLLA, ABS, PCL Composites  | PLA, ABS, PCL, PLGA, EPO, EVA Composite | PLA, ABS, HIPS, PMMA                             |
| Equipment                    | <sup>(1)</sup> Customized and<br><sup>(2)</sup> Commercial (RegenHU)        | Customized                              | Customized                                       |
| References                   | [33–36, 41]   | [37, 39, 42–44]                         | [29, 40, 45]                                     |

its applicability to biomedical applications. However, the HE design also has its drawbacks, such as lower printing quality and limited material flexibility. Furthermore, there is a lack of studies in the literature investigating the use of the HE design for 3D printing scaffolds using low-melting point biomaterials like PCL.

To address these limitations while capitalizing on the advantages of the HE design, this study proposes modifications to enhance its performance, primarily focusing on the screw and barrel designs, as well as the selection of their materials. These modifications aim to overcome the drawbacks of the HE design while further improving its merits for the fabrication of scaffolds, especially using low-melting point biomaterials such as PCL.

## 2.2 DPSE printer head design

Figure 2a provides an overview of the 3D view of the DPSE, while Fig. 2b presents a sectional view of the DPSE printer head. The DPSE design uses available components from commercial c-FDM-based printers, including a hot-end block, connector, cooling fan, and a 0.4-mm nozzle (specifically, the 3D Anycub i3 Hotend V5 J-head model).

Other essential parts, such as the hopper, barrel and screw, were designed and manufactured to complement these components. The hopper, fabricated using a c-FDM 3D printer, was constructed using PLA material. To facilitate easy assembly and cleaning processes, specifically to ensure effective heat transfer control, the machined barrel was divided into two distinct parts: top and bottom barrels. These two sections were alternated using two different materials, namely, aluminum and Teflon. In addition, O-rings were incorporated on the inside of the top barrel to regulate heat transfer and connected to the screw, as shown in Fig. 2b. The number and thickness of these O-rings, made

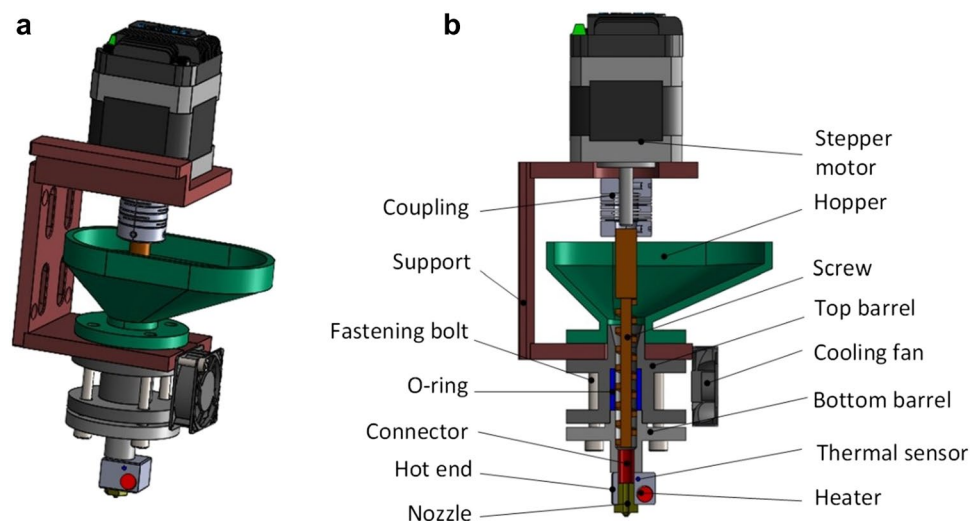
from either aluminum or Teflon, can be adjusted to control the heat transfer. The power heater of 50 W and the PT100 temperature sensor was mounted on the hot end. A proportional-integral-derivative (PID) temperature controller was utilized to regulate the printing temperature precisely. The hot end and the bottom barrel were connected using an M6 connector thread. Unlike previous studies reported in the literature, no complex cooling system is required for this customized DPSE except for a regular cooling fan.

## 2.3 Thermal analysis using FEM

Within the framework of a screw-based powder 3D printer, the screw is designed to comprise three distinct regions: feed, compression, and melt. Despite the melting point of PCL material being 60 °C, it is observed that operating within an intermediate temperature range of 55–65 °C induces a pre-melt state in which the PCL powder material undergoes partial melting, softening, and adhering to the screw surface, called the sticky state. If this state persists within the top barrel, it forms a material slurry that may cause adhesion and clogging issues in the compression and feed regions. Consequently, it is imperative to eliminate this sticky state within the top barrel to prevent such material-related complications. As a result, the material within the feed and compression regions remains in a powder state, effectively minimizing the accumulation of dead waste material.

The Siemens Star CCM + Thermal Analysis software is used to examine the thermal heat flow within the barrel under different design conditions. The primary objective of this analysis is to comprehensively understand the heat transfer dynamics occurring inside the barrel, particularly in ensuring that heat is concentrated only in the melt region. Furthermore, it is essential to maintain the temperature

**Fig. 2** The assembly model of the developed DPSE printer head in 3D view (a) and section view (b)





within the compression and feed regions below the intermediate temperature threshold. The analysis includes four distinct study cases that correspond to various material combinations for the key components of the DPSE, including the top barrel, bottom barrel, screw, and O-rings, as presented in Table 2.

The numerical modeling analysis was employed to simulate the mechanical-thermal behavior of the feeding screw. The main material parameters utilized in the finite element method (FEM) analysis that are presented in Table 3.

The ambient temperature was set at 25 °C for the simulations. By varying the material properties of the screw, top barrel, and O-ring, the heat distribution inside the barrel exhibited variations, as depicted in Fig. 3. Case 1 and Case 2 were examined to compare the heat transfer inside the barrel when using aluminum and Teflon for the top barrel, respectively. Figure 3a demonstrates that in Case 1, the heat is dispersed throughout most parts of the extruder due to the high thermal conductivity of aluminum. Consequently, the complete formation of the melt region is hindered, while the compression and feed regions are in the intermediate temperature range, resulting in the PCL material being in a sticky state that prevents efficient extrusion through the printing nozzle.

Employing the Teflon top barrel and aluminum O-rings in Case 2 shows different heat distributions across distinct regions, as depicted in Fig. 3b. The melt region is formed; however, this region is quite broad, overwhelming the compression region and approaching the feed region. Consequently, the heat could eventually transfer to the entire feed region after a prolonged printing time. The O-rings were replaced with Teflon material in Case 3 to reduce the size of the melt region (Fig. 3c). As observed, the melt region was reduced, while the intermediate temperature region remained significant. Therefore, the stainless-steel screw

was substituted with a Teflon screw with a steel core in Case 4, as shown in Fig. 3d. This modification significantly restricted the intermediate temperature region, which only existed in the small interface region between the top and bottom barrels.

Further details of the temperature distribution are presented in Fig. 4. Specifically, in Case 4 (Fig. 4b), the high temperature was concentrated only on the first two pitches of the screw, in contrast to Case 3 with the stainless steel screw (Fig. 4a), where the high temperature extended up to the first four pitches. As the temperature in the compression and feed regions remained below 40 °C, the PCL material maintained its original powder state, which is ideal for the powder extrusion process. This can be attributed to the excellent insulation properties of the Teflon material used in the screw. The mechanical-thermal behavior of the screw is summarized in Table 4. The modeling results indicate a slight displacement of the Teflon screw with a steel core compared to the stainless-steel screw, attributed to the thermal effects from the heating process, which ideally does not impact the screw performance. Based on the numerical modeling analysis, the design in Case 4 was adopted for the DPSE, as it fulfilled the requirements of minimizing heat transfer upward and reducing the amount of dead material, thereby enabling the fabrication of the experimental printer head.

## 3 Materials and experimental methods

### 3.1 Materials and printing setup

PCL powder (Mw 50,000) below 500  $\mu\text{m}$  powder size was supplied by Polysciences, Warrington, PA, USA. Three filler types include SA powder (natural polymer, CAS 9005–38-3, Thermo Scientific). PEG powder (thermoplastic polymer,

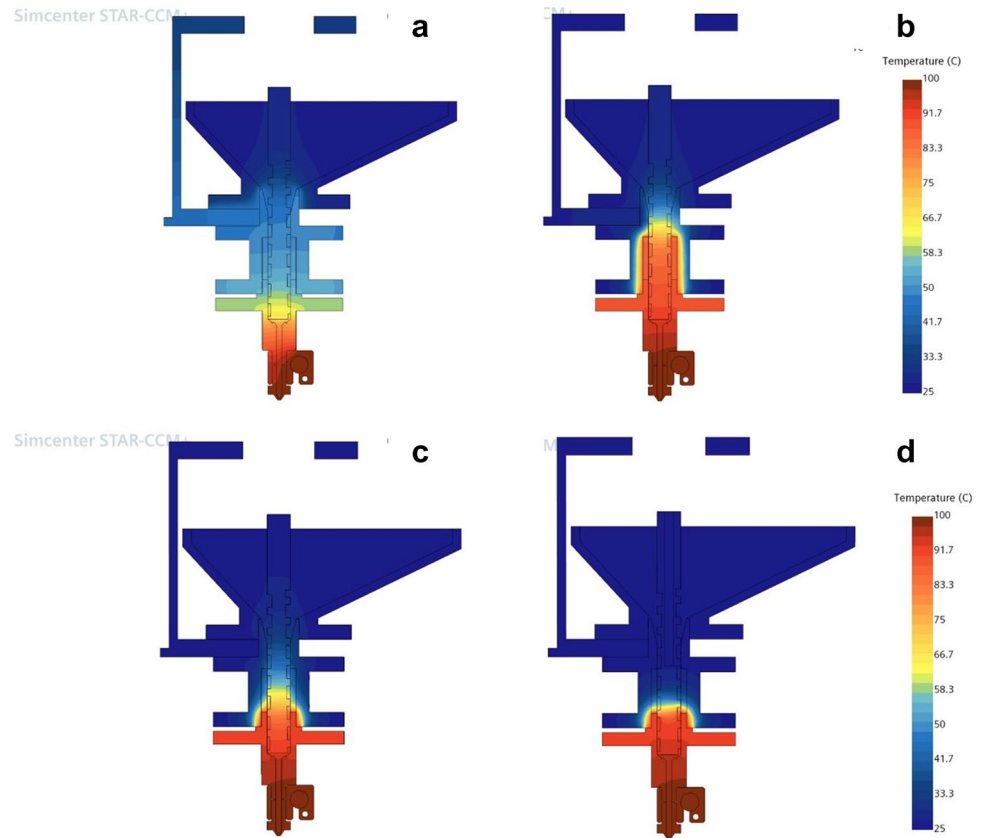
**Table 2** The material combinations for FEM analysis

| Case study   | Top barrel | Bottom barrel | Screw                  | O-rings  |
|--------------|------------|---------------|------------------------|----------|
| Case 1: AASA | Aluminum   | Aluminum      | Stainless steel        | Aluminum |
| Case 2: TASA | Teflon     | Aluminum      | Stainless steel        | Aluminum |
| Case 3: TAST | Teflon     | Aluminum      | Stainless steel        | Teflon   |
| Case 4: TATT | Teflon     | Aluminum      | Teflon with steel core | Teflon   |

**Table 3** Material properties for FEM analysis

|   | PCL                  | Aluminum              | Stainless steel       | Teflon               |
|---|----------------------|-----------------------|-----------------------|----------------------|
| Density ( $\text{kg}/\text{m}^3$ )  | 1145                 | 2702                  | 8055                  | 2140                 |
| Specific heat ( $\text{J}/(\text{kg} \cdot ^\circ\text{C})$ )                   | 4181                 | 903                   | 480                   | 1000                 |
| Melting point ( $^\circ\text{C}$ )  | 60                   | 660                   | 1230                  | 327                  |
| Thermal expansion ( $1/^\circ\text{C}$ )  | $2.3 \times 10^{-4}$ | $24.0 \times 10^{-6}$ | $1.72 \times 10^{-5}$ | $1.5 \times 10^{-4}$ |
| Thermal conductivity coefficient ( $\text{W}/(\text{m} \cdot ^\circ\text{C})$ ) | 0.62                 | 237                   | 15.1                  | 0.25                 |

**Fig. 3** Heat distribution in the barrel in different designs using numerical modeling in Case 1, AASA (a); Case 2, TASA (b); Case 3, TAST (c); and Case 4, TATT (d)

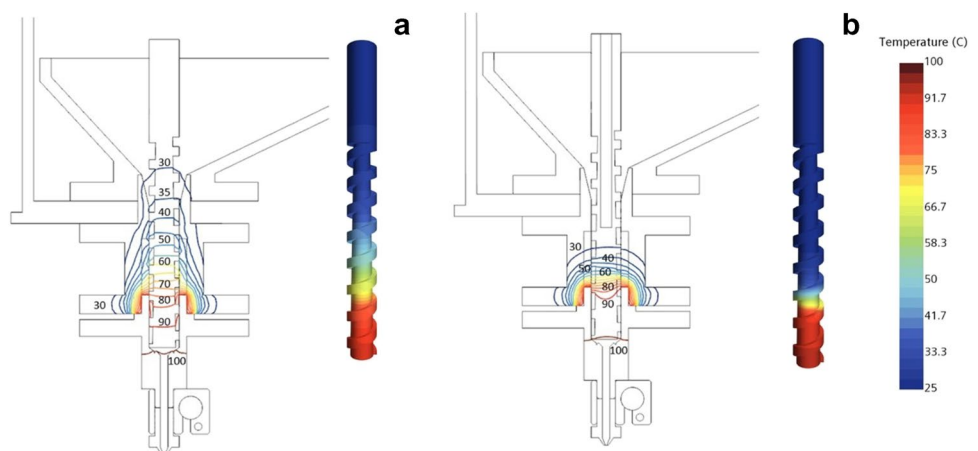


CAS 25322–68-3, Shanghai Zhanyun Chemical Co.Ltd.) and TCP powder (ceramic, CAS 7758–87-4, Shanghai Zhanyun Chemical Co.Ltd.) were mixed with PCL powder at a 20 wt% ratio. Additionally, a higher filler ratio of 40 wt% was employed specifically for the ceramic additive to assess its printability.

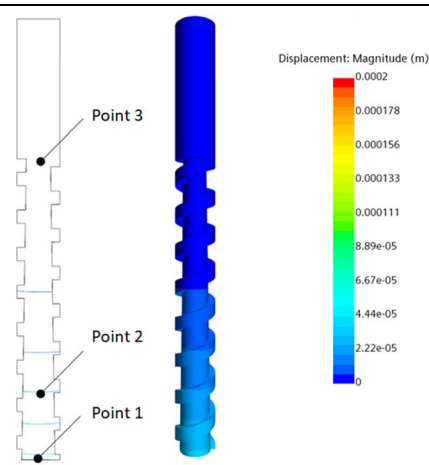
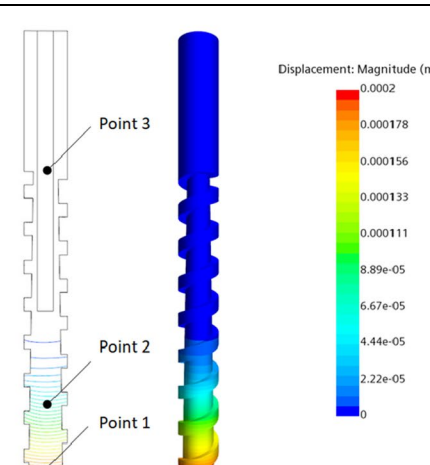
The powder mixtures were prepared according to the following formulations: pure PCL (PCL0), pure PEG (PEG0), 80%PCL-20%PEG (PCL-20PEG), 80%PCL-20%SA (PCL-20SA), 80%PCL-20%TCP (PCL-20TCP), and 60%PCL-40%TCP (PCL-40TCP). After thoroughly mixing

to achieve a homogeneous powder state, the powder mixture was directly loaded into the hopper and subsequently transferred to the nozzle through the screw mechanism. The scaffold printing process was conducted using a 0.4-mm-diameter nozzle, with a line spacing of 0.8 mm and a layer thickness of 0.35 mm. Figure 5 a and b depict the DPSE printer head components and assembly, respectively. Figure 5c illustrates the DPSE printer head mounted at one of the four positions on the customized multi-head 3D printer designed for biofabrication applications. Customized software was employed to generate G-code automatically and

**Fig. 4** The temperature isoline in the barrel and heat distribution on the screw in Case 3 (a) and Case 4 (b)



**Table 4** Thermal deformation of the screw

|                    | Displacement Case 3 (m)   | Displacement Case 4 (m)  |
|--------------------|---|--|
| Simulation results |  |  |
| Point 1            | $3.217 \times 10^{-5}$  | $1.862 \times 10^{-4}$   |
| Point 2            | $1.803 \times 10^{-5}$  | $5.689 \times 10^{-5}$   |
| Point 3            | $1.141 \times 10^{-6}$  | $2.312 \times 10^{-8}$   |

control the DPSE printer system. Figure 5 d, e, and f show PCL0, PCL-40TCP, and PCL-20SA specimens during the printing process, respectively. The addition of TCP into the PCL material induces a color change from clear white to opaque white, while the incorporation of SA in the PCL scaffold results in a color change from white to light yellow.

### 3.2 Printability and scaffold characteristic investigation

Several fundamental scaffold characteristics, including surface morphology, hydrophilicity, chemical characterization, scaffold porosity, mechanical properties, and cell attachment, were investigated to determine the applicability of PCL-based scaffold fabricated by the DPSE printer head for tissue engineering. Additionally, an evaluation of the printing conditions and accuracy was conducted for each PCL-based composite to determine the printability of the composites as well as the material flexibility of DPSE.

#### a) Scaffold morphology and surface roughness

The top view of each PCL-based scaffold was analyzed using optical microscopy, while scanning electron microscopy (SEM) was used to produce images of the

3D scaffold cross-section view. The 3D laser scanning microscope VK-X1000 Keyence was used to capture the surface roughness of the PCL-based scaffold and each printed line.

#### b) Water contact angle measurement

The hydrophobicity of PCL-based composite scaffolds was determined by measuring the static water contact angle at room temperature. Briefly, 5  $\mu\text{l}$  of a deionized water droplet was pumped onto the top of the scaffold using a Hamilton micro syringe. The images of the droplets were recorded by a high-speed camera Shodensha CHU-30C, Japan, and processed by ImageJ software. The contact angle was measured at different time points.

#### iii) ATR analysis

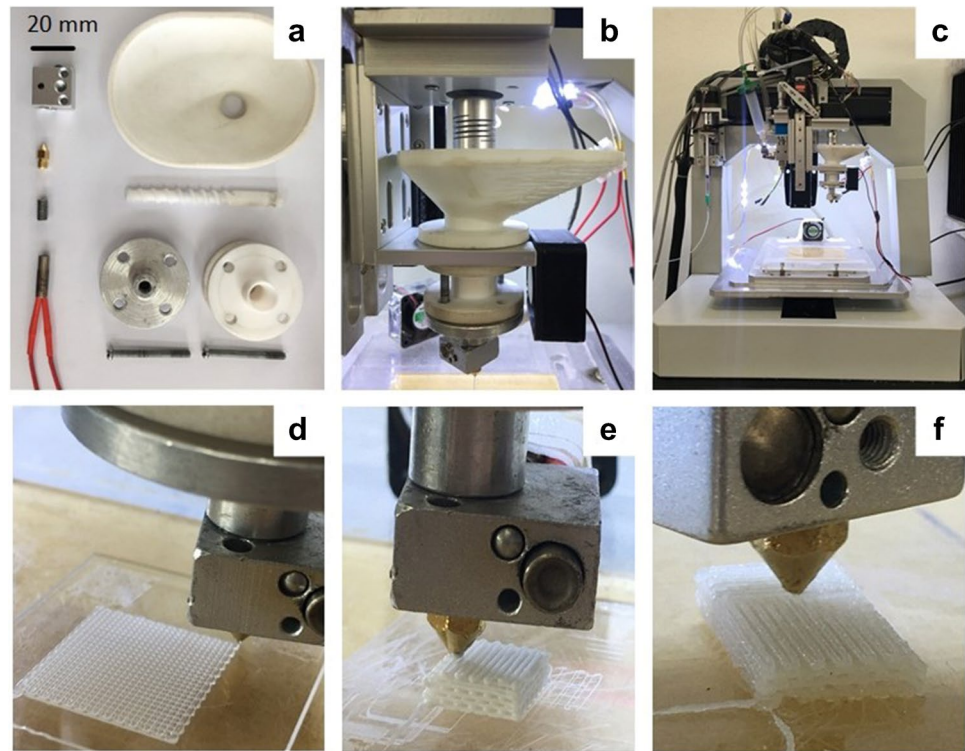
Functional groups of different PCL-based composites were analyzed by attenuated total reflection Fourier-transform infrared (ATR-FTIR, Perkin-Elmer Spectrum Spotlight-400). Measurements were conducted over 32 scans at a resolution of  $2 \text{ cm}^{-1}$  using ambient air as the background.

#### iv) Scaffold porosity

Scaffold porosity was determined by a gravimetric method [3]. Each sample ( $n=3$ ) was weighted to determine the mass and measured the dimension of printed scaffolds



**Fig. 5** Photos of **a** the components of the DPSE printer head, **b** an assembled DPSE printer head, **c** the assembly of the DPSE printer head onto a multi-head customized 3D printer, **d** PCL0 printing specimen using PCL0, **e** PCL-40TCP printing specimen, and **f** the PCL-20SA printing specimen



to obtain the volume. The porosity was determined as follows:

$$\rho_{\text{scaffold}} = \frac{\text{mass}}{\text{volume}} \quad (1)$$

$$\rho_{\text{material}} = F_{\text{PCL}} * \rho_{\text{PCL}} + F_{\text{filler}} * \rho_{\text{filler}} \quad (2)$$

$$\text{Porosity}(\%) = \left( 1 - \frac{\rho_{\text{scaffold}}}{\rho_{\text{material}}} \right) * 100 \quad (3)$$

where  $\rho_{\text{scaffold}}$  is the density of the scaffold and  $\rho_{\text{material}}$  the density of the composite using the theoretical density of PCL ( $\rho_{\text{PCL}} = 1.145\text{g/cm}^3$ ) and filler ( $\rho_{\text{filler}} : \rho_{\text{PEG}} = 1.125\text{g/cm}^3, \rho_{\text{TCP}} = 3.14\text{g/cm}^3, \rho_{\text{SA}} = 1.0\text{g/cm}^3$ ).  $F_{\text{PCL}}$  and  $F_{\text{filler}}$  indicate the weight fractions in the composite.

#### e) Mechanical properties of PCL-based scaffolds

Mechanical properties of various PCL-based scaffolds were evaluated through compression and tensile tests. For the compression test, PCL-based scaffolds with dimensions of 10 mm width  $\times$  10 mm length  $\times$  8.5 mm depth were subjected to crushing using an MTS compression testing machine model E45, employing a cross-head speed of 1 mm/min. Tensile testing was conducted on porous bone-shaped samples measuring 50 mm length  $\times$  10 mm width  $\times$  2 mm depth, with a gauge width of 4 mm and a gauge length of 20 mm,

utilizing the GOTECH AI-7000-M machine. The tensile test followed the specifications outlined in ASTM D638, employing a cross-head displacement rate of 50 mm/min.

#### f) Cell attachment on 3D scaffolds

Cell attachment experiments were conducted using cylindrical porous scaffolds, which were obtained by punching out structures from the 3D-printed scaffold with the 0°/45°/90°/135° laydown pattern. The cylindrical scaffolds had dimensions of 4.4 mm in diameter, 2.7 mm in height, macropore size of 0.4 mm, and a line width of 0.4 mm. All materials and mediums used for cell culture were purchased from Sigma-Aldrich. Before seeding the cell, the scaffolds were pre-coated with gelatin 0.2% and then incubated with cell culture medium for 2 h. Human lung fibroblasts were grown in Dulbecco's modified Eagle's medium (DMEM) supplemented with 10% fetal bovine serum and 1% penicillin–streptomycin and cultured in a cell incubator at 37 °C in 5% CO<sub>2</sub>. A total of 100,000 cells in 20  $\mu\text{L}$  cell culture medium were seeded onto the scaffolds and incubated in the incubator for 1 h before adding 150  $\mu\text{L}$  culture medium. Cell attachment was evaluated at 3 days with fluorescein diacetate (FDA). Briefly, 10  $\mu\text{g/mL}$  final concentration of FDA was added onto cells and maintained in a serum-free medium for 5 min at room temperature in the dark. The staining solution was removed and rinsed with phosphate-buffered saline. The cell adhesion and cell morphology were observed using a fluorescence microscope.

### g) Printing condition investigation

A series of experiments using various printing conditions were conducted to investigate the printability and printing accuracy of PCL-based composites. The printing temperature, printing speed, and extrusion speed were systematically varied to explore their impact on the printing process. Specifically, three different printing temperatures of 90 °C, 100 °C, and 110 °C were evaluated; the printing speed was incrementally adjusted from 2 to 10 mm/s, while the extrusion speed was varied between 8 and 17 rpm, depending on the specific PCL-based composite tested. The specimens had the 0°/90° lay-down pattern, and both the line width and pore size were maintained at 0.4 mm. A comprehensive overview of the different printing conditions can be found in Table 5, providing detailed information on each parameter variation.

**Table 5** Printing conditions for PCL-based composites

|                      |  |
|----------------------|--|
| 3D Printer           | Customized 3D printer with DPSE printer head   |
| Printing materials   | PCL0 (Pure PCL)<br>PEG0 (Pure PEG)<br>PCL-20PEG (80%PCL-20%PEG)<br>PCL-20SA (80%PCL-20%SA)<br>PCL-20TCP(80%PCL-20%TCP)<br>PCL-40TCP (60%PCL-40%SA) |
| Printing temperature | 90°C, 100°C, and 110°C   |
| Printing speed       | 2–10 mm/s (varied with materials)  |
| Extrusion speed      | 8–17 rpm (varied with materials)   |
| Desired line width   | 0.4 mm   |

## 4 Experimental scaffold printing results and discussions

### 4.1 Amount of material consumables

The DPSE design exhibits a notable benefit in its capacity to minimize the input materials and reduce the post-printing waste material. Figure 6a shows the image of the screw with three distinct regions after a four-hour printing. Moreover, Fig. 6b illustrates the presence of a melt region exclusively at the last two pitches of the screw. This observation is consistent with the numerical modeling analysis that was conducted for the Case 4 design. The compression region (Fig. 6c) was entirely coated with a compressed PCL powder covering the pitches of the screw. The powdered material tends to dislodge from the feed region upon removing the screw from the barrel (Fig. 6d). After printing, all remaining materials, encompassing powdered and molten forms, were carefully removed and weighed. The quantity of materials in different locations is documented in Table 6. Remarkably, the printing process commences with only 1.22 g of initial material requirement, while the waste material constitutes nearly half of that (0.57 g). Importantly, the remaining material in the compression and feed regions along the screw, which remains powdered, can be effectively reused for subsequent printing processes. Experimental findings further demonstrate that the DPSE printer head can continuously print for extended durations without encountering heat transfer problems in the hopper. This is achieved by implementing a simple cooling method employing a fan.

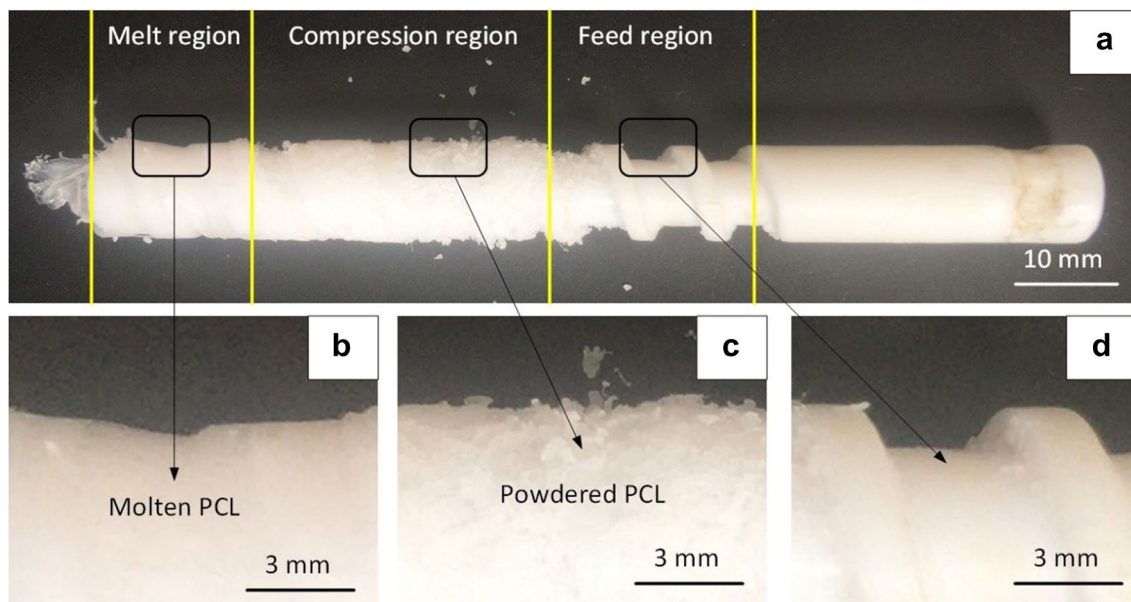


**Fig. 6** The picture of the Teflon screw after printing (a) with the melt region (b), compression region (c), and feed region (d)

**Table 6** Amount of material consumables for PCL0 printing

| Material region                          | Amount (g) | Note   |
|--|------------|--|
| Reusable material                        | 0.57       | The remaining material under powder state after printing |
| Waste material at the end of the screw   | 0.15       | Molten material  |
| Waste material inside the bottom barrel  | 0.46       | Molten material  |
| Waste material inside the nozzle         | 0.04       | Molten material  |
| Minimum material amount at the beginning | 1.22       | Material under powder state                              |
| Material amount for specimen             | -          | Depending on specimen                                    |

## 4.2 Printability and scaffold characteristic results

### a) Scaffold morphology and surface roughness

The morphology of the printed line varies among different PCL-based composites when a scaffold line width (SLW) of 0.4 mm is considered, as shown in Fig. 7. The clear and well-defined printed lines are observed in both PCL0 and PCL-20PEG specimens (Fig. 7 a and c). Conversely, other composite specimens display the presence of additive powders. The PEG0 specimens exhibited satisfactory printability, as shown in Fig. 7b. However, they are prone to breaking upon exposure to light impact, indicating that using pure PEG material is not recommended for scaffold printing. In the case of PCL-20SA, the printed lines displayed a highly rough surface, which can be attributed to the propensity of SA powder to undergo swelling and clustering during the printing process. As observed in Fig. 7d, the swollen SA powder can be observed on the printed line interior and

exterior, further accentuating the surface roughness. The uniform distribution of TCP powder is observed along the printed lines of both PCL-20TCP and PCL-40TCP composites. Comparatively, a higher concentration of TCP powders can be observed in the PCL-40TCP specimen (Fig. 7f) than in the PCL-20TCP specimen (Fig. 7e). A uniform distribution of TCP powder was observed on the surface of the scaffold.

To gain further insights, Fig. 8 presents SEM images of cross-section views at different resolutions for four representative scaffold types, namely, PCL0, PCL-20PEG, PCL-20SA, and PCL-40TCP. Interconnected pores that are well-fabricated can be observed throughout the depth of the scaffolds. Specifically, Fig. 8a illustrates the straight and uniform printed line width of the PCL0 scaffold, while Fig. 8b displays a considerable variation in the printed line width of the PCL-20PEG scaffold. The swelling phenomenon of SA powder is evident in the cross-section view of the PCL-20SA printed line, as observed in Fig. 8 c and g. This swelling property, in

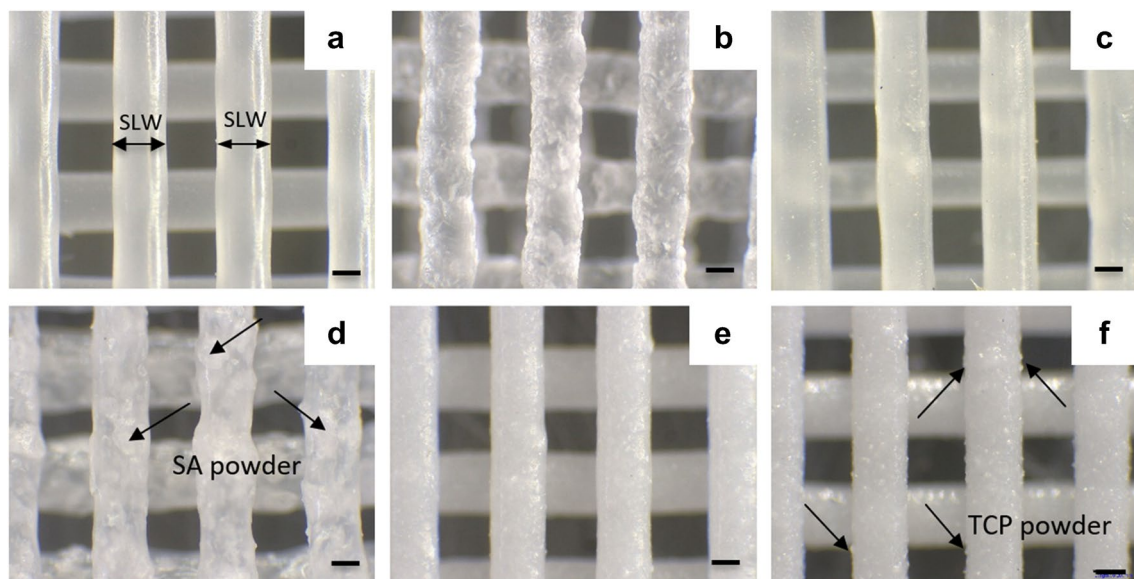


**Fig. 7** The optical microscopy images showing the top view of PCL0 scaffold (a), PEG0 scaffold (b), PCL-20PEG scaffold (c), PCL-20SA scaffold (d), PCL-20TCP scaffold (e), and PCL-40TCP scaffold (f). Scale bar 200  $\mu$ m



conjunction with the presence of SA powders, contributes to a decreased consistency of the printed line. Furthermore, it can be observed that TCP powders are visible both internally and externally on the printed line, as shown in Fig. 8h.

The surface roughness and morphology play a crucial role in influencing cell behavior and protein absorption [22]. As observed in Fig. 9, introducing additives significantly increases the surface roughness. The 3D profiles were captured to evaluate the topographical features of each composite specimen. The results revealed that the height (peak-to-valley view) of the scaffold surface with fillers differed compared to the pure PCL scaffold, as indicated by the Rz values. Additionally, the Ra values, representing the arithmetic average of the roughness profile, were determined to quantify the differences in surface roughness among the specimens. The Ra values of PCL-PEG and PCL-SA scaffolds were significantly higher than those of pure PCL and PCL-TCP scaffolds. However, no significant difference in Ra values was observed between PCL and PCL-TCP specimens. Interestingly, the composite scaffolds exhibited a significantly higher Sa value, which measures the height difference of each point relative to the arithmetic mean of the surface.

Based on these results, it can be concluded that the inclusion of additive results in a significant increase in surface roughness. Previous studies have reported that cells exhibited more

favorable responses to PCL-based composite scaffolds with increased surface roughness [46, 47]. For example, the PCL scaffold with an average roughness of  $56.42 \mu\text{m}$  (Sa) exhibited a positive effect on cell growth and differentiation, and this effect was observed to increase with the increase of surface roughness [47]. These findings suggested that PCL composite scaffolds exhibit the potential to promote desired cell behaviors. Furthermore, the 3D profiles also indicated that the additives are evenly distributed across the entire surface area of the scaffolds.

## b) Hydrophobicity properties

The surface wettability and material hydrophobicity of the PCL-based scaffolds were evaluated using water contact angle measurements. Figure 10 presents the water contact angle values before and after dropping water on the sample surface at 0, 3, and 30 s. The PCL0 scaffold surface exhibited the highest contact angle value of  $113^\circ$  at 0 s, which decreased to  $106^\circ$  after 30 s of water droplet deposition, indicating its hydrophobicity. Remarkably, the addition of various fillers, such as PEG, SA, or TCP, into the pure PCL matrix led to a decrease in the contact angle values. This observed decrease indicates an improvement in the hydrophilicity of the PCL scaffold with the incorporation of these fillers.

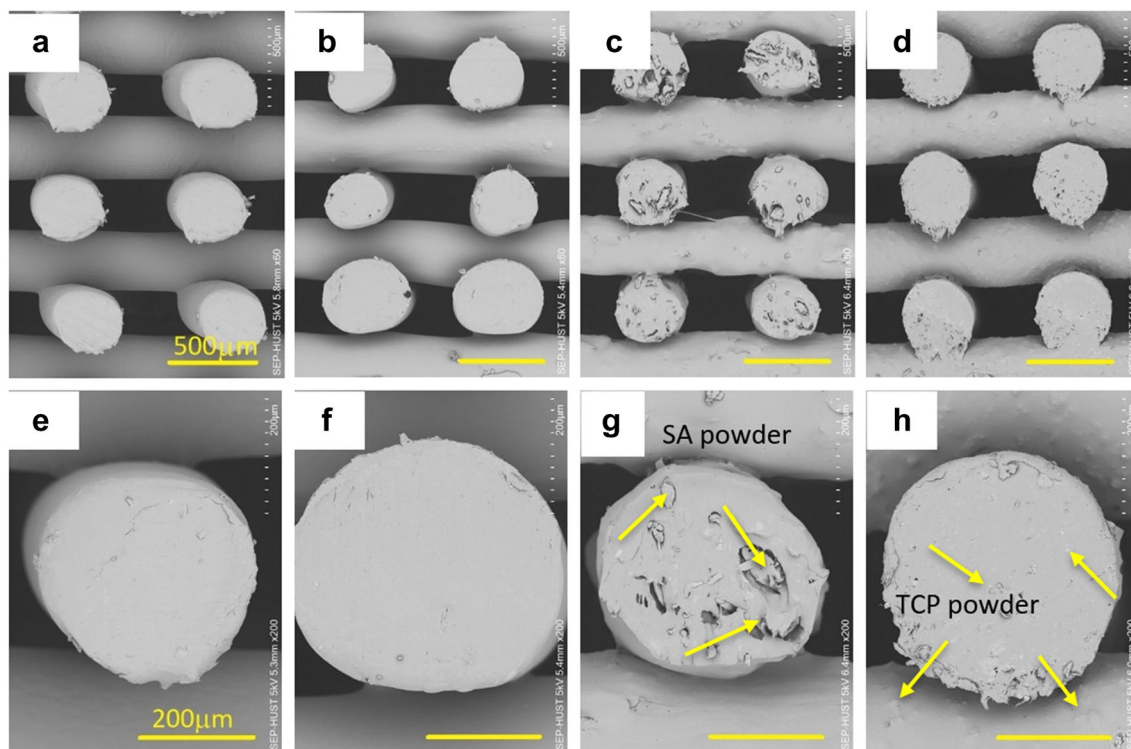


**Fig. 8** SEM images of a cross-section view of the PCL0 scaffold (a), PCL-20PEG (b), PCL-20SA scaffold (c), and PCL-40TCP scaffold (d) (scale bar  $500\mu\text{m}$ ) and cross-section view of the PCL0 line (e)

PCL-20PEG line (f), PCL-20SA line (g), and PCL-40TCP line (h) (scale bar  $200\mu\text{m}$ )

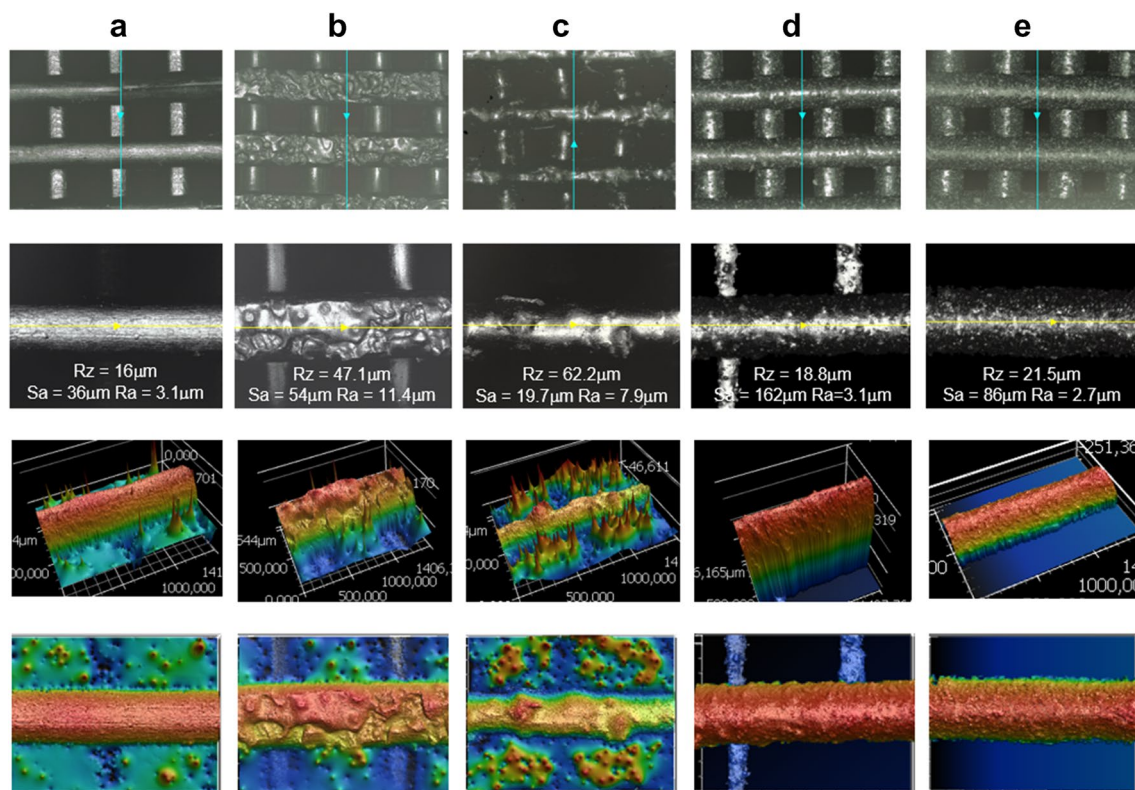


**Fig. 9** The scaffold morphology and surface roughness obtained using a laser scanning microscope of PCL0 (a), PCL-20PEG (b), PCL-20SA (c), PCL-20TCP (d), and PCL-40TCP (e)

At the time of contact with the scaffold surface, it has been observed that the PCL-20PEG scaffold has a relatively high water contact angle of  $97^\circ$ . However, this angle significantly decreased to  $55^\circ$  after 3 s, and the water droplet was completely absorbed into the scaffold after 4 s, as illustrated in Fig. 10b. Conversely, the PCL-20SA scaffold displayed a low water contact angle of  $52^\circ$  at 0 s, which further reduced to  $31^\circ$  following 30 s of droplet deposition, as shown in Fig. 10c. The incorporation of TCP into the scaffold reduced hydrophobicity of the PCL matrix. This effect was more pronounced with higher TCP content, as depicted in Fig. 10 d and e. These findings agree with the observations of increased surface roughness in the composite scaffolds. According to previous reports, enhanced surface hydrophilicity facilitated cell adhesion, proliferation, and differentiation [48, 49]. Therefore, it is reasonable to conclude that PCL composite scaffolds can promote these cell behaviors through their improved surface hydrophilicity.

iii) ATR analysis

The ATR-FTIR spectra of different samples are summarized in Fig. 11. The PCL0 scaffold exhibited fingerprint absorption bands of C=O groups at  $1720\text{ cm}^{-1}$ , C–O–C vibrational stretching at  $1238\text{ cm}^{-1}$ , C–C stretching at  $1292\text{ cm}^{-1}$ , and CH<sub>2</sub>-CH<sub>2</sub> groups at  $2937\text{ cm}^{-1}$ . The spectrum of PEG0 powder displayed

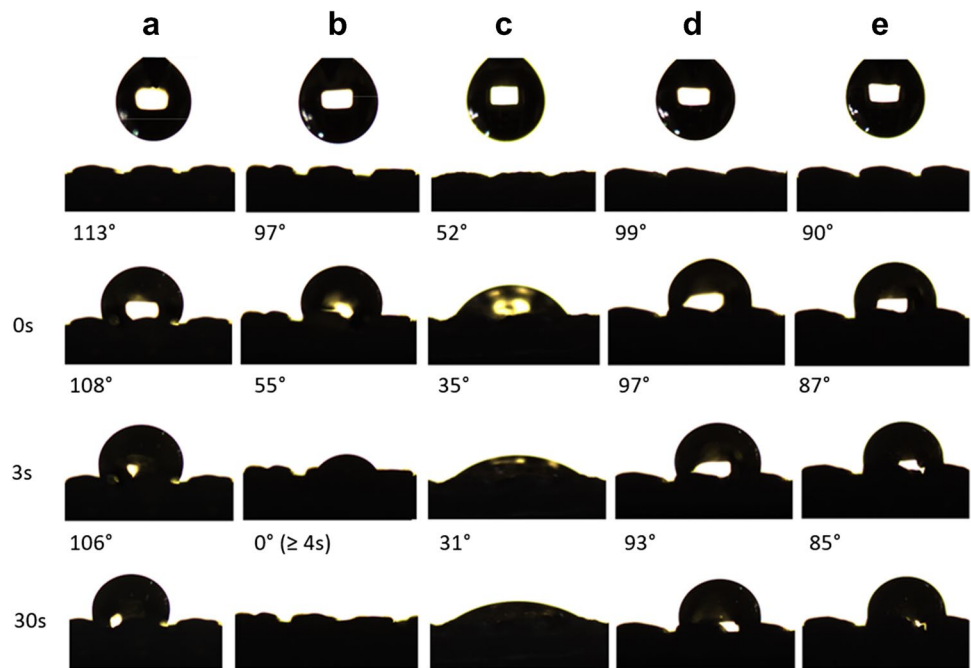
typical peaks at  $1108\text{ cm}^{-1}$  of C–O–C vibrational stretching,  $1060\text{ cm}^{-1}$  (C–OH vibrational stretching), and  $2883\text{ cm}^{-1}$  (CH<sub>2</sub>-CH<sub>2</sub> vibrational). Absorption bands at about  $964\text{ cm}^{-1}$  and  $840\text{ cm}^{-1}$  were the typical bands of the PEG crystal phase [50]. Characteristics of both PCL and PEG fragments were presented in the PCL-PEG composite as shown in Fig. 11a.

ATR-FTIR spectrum of SA spectra revealed a significant absorption band of the OH- functional group in the range of  $3600\text{--}3100\text{ cm}^{-1}$ . In addition, the stretching vibrations of the COO-groups were identified as absorption bands at about  $1595\text{ cm}^{-1}$  and  $1410\text{ cm}^{-1}$  [51, 52]. The absorption band at about  $1024\text{ cm}^{-1}$  is assigned to C–C stretching [52]. The ATR-FTIR of the PCL-SA composite scaffold in Fig. 11b exhibited the fingerprint peaks of both SA and PCL. It should be noted that the peak observed at  $1024\text{ cm}^{-1}$ , which is attributed to the C–C stretching in the SA sample, has the potential to be superimposed by the PCL peak.

The TCP powder sample showed absorption bands assigned to the  $\text{PO}_4^{3-}$  at  $561\text{ cm}^{-1}$  ( $\nu_4$ ),  $600\text{ cm}^{-1}$  ( $\nu_4$ ),  $963\text{ cm}^{-1}$  ( $\nu_1$ ), and  $1019\text{ cm}^{-1}$  ( $\nu_3$ ) [53, 54]. The printed PCL-TCP scaffold included the typical bands of TCP (i.e.,  $\text{PO}_4$  groups at about 561, 600, 963 and  $1019\text{ cm}^{-1}$ ) in addition to PCL fingerprint bands in Fig. 11c.



**Fig. 10** Water contact angle of a water droplet on different scaffold surfaces of PCL0 (a), PCL-20PEG (b), PCL-20SA (c), PCL-20TCP (d), and PCL-40TCP (e) before dropping, 0 s, 3 s, and 30 s



#### iv) Scaffold porosity

The PCL-based scaffolds exhibited 100% interconnectivity and an overall porosity of 41–46% regardless of the additive used with a macropore size of 390–410  $\mu\text{m}$ . Specifically, the porosity of PCL0, PCL-20PEG, PCL-20SA, PCL-20TCP, and PCL-40TCP were determined  $46.6 \pm 0.5$ ,  $46.8 \pm 0.9$ ,  $46.4 \pm 0.4$ ,  $44.7 \pm 0.6$ , and  $41 \pm 0.7$ , respectively. The designed scaffold has a porous structure with a pore size of 0.4 mm and line width on the plane and 0.35 mm pore size on depth and a porosity of 53%. The overlap depth, which decreases the pore size in depth, accounts for the different porosity values between printed scaffolds and designed scaffolds.

#### e) Mechanical properties

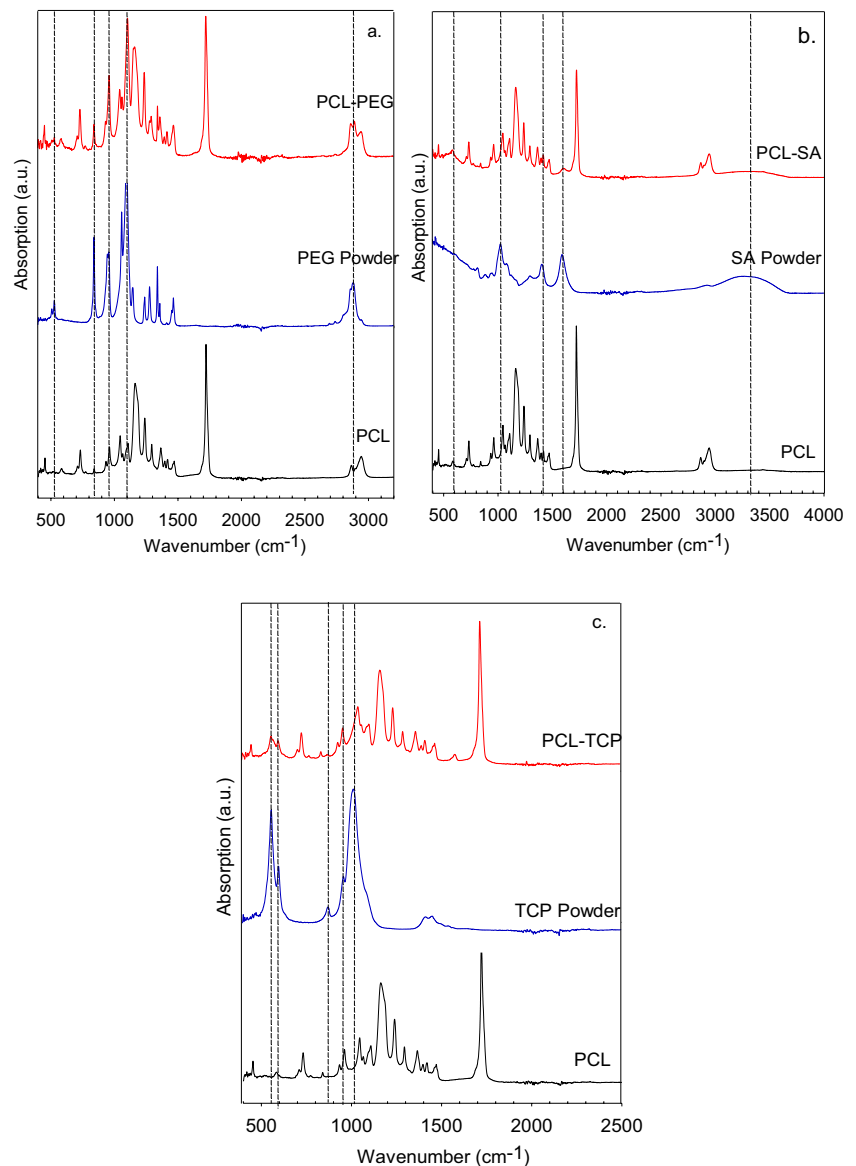
The specimens used for the compression test and tensile test are shown in Fig. 12 a and b, respectively. The experimental results were obtained by recording the load–displacement measurements and computing the stress–strain data. The compressive modulus was determined from the elastic region of the compression stress–strain curve (Fig. 12c). The tensile stress–strain curve (Fig. 12d) was analyzed to obtain the tensile strength at break. The results indicated that the addition of SA and PEG significantly decreases the compression modulus of the pure PCL scaffold. On the contrary, the inclusion of TCP generally increases the compression modulus of the scaffold, with the highest value of  $86.6 \pm 9.7$  MPa observed at a TCP content of 40 wt%. The TCP phase, characterized by a family of hexagonal unit cells, exhibits excellent compression strength, enhancing the compression modulus (Fig. 12e). In addition, the low porosity of the PCL-40TCP scaffold is also

attributed to the high compression modulus in this study. The lower compressive modulus of the PCL-20PEG and PCL-20SA scaffolds can be attributed to the lower modulus of these materials compared to PCL0. However, it should be noted that the compression modulus of all scaffolds falls within the suitable range for bone tissue engineering applications. This ranges typically from 10 to 500 MPa depending on the specific type of bone tissue [55, 56]. Fig. 12 Mechanical property comparison of PCL-based composite specimens: compression test specimens (a); tensile test specimens (b); compression stress and strain curves (c); tensile stress and strain curves (d); compression modulus (e); and tensile strength (f) for PCL-based scaffolds. Scale bar 10 mm

The tensile stress–strain curve in Fig. 12d indicated that the PCL0 experienced a long oscillating period while deforming. This is explained by the combination of the hardening phenomenon and the slippage of the molecular chains. The hardening phenomenon of PCL0 is caused by the crystallization induced by strain/stress, which forms a highly oriented crystalline phase in PCL0 and subsequently increases the tensile strength of PCL0 during deformation [57]. Therefore, before rupture, PCL0 has a light hardening phenomenon, resulting in a marginally elevated stress at the break compared to the stress in the plastic deformation period. On the contrary, PEG and SA have a lower density of rigid carboxyl group in their backbone; therefore, the tensile test results indicated that PCL-20PEG and PCL-20SA exhibited lower tensile strength, as shown in Fig. 12f.

Incorporating the ceramics phase into the polymer phase changes the stress–strain behavior of the scaffold at a high TCP content of 40 wt%. As a result, the tensile stress–strain curve of the PCL-40TCP sample (blue line on Fig. 12d) shows a linear

**Fig. 11** ATR-FTIR spectra of different samples for PCL-PEG scaffold (a), PCL-SA scaffold (b), and PCL-TCP (c)



elastic behavior leading to failure without plastic deformation, which is the typical stress–strain curve of the ceramic material. However, the stress–strain behavior of the PCL-20TCP scaffold exhibited three regions similar to those of the PCL scaffold (purple line on Fig. 12d) when TCP content was low at 20 wt%. This plastic behavior can be explained by the PCL phase due to the low TCP content in the composite.

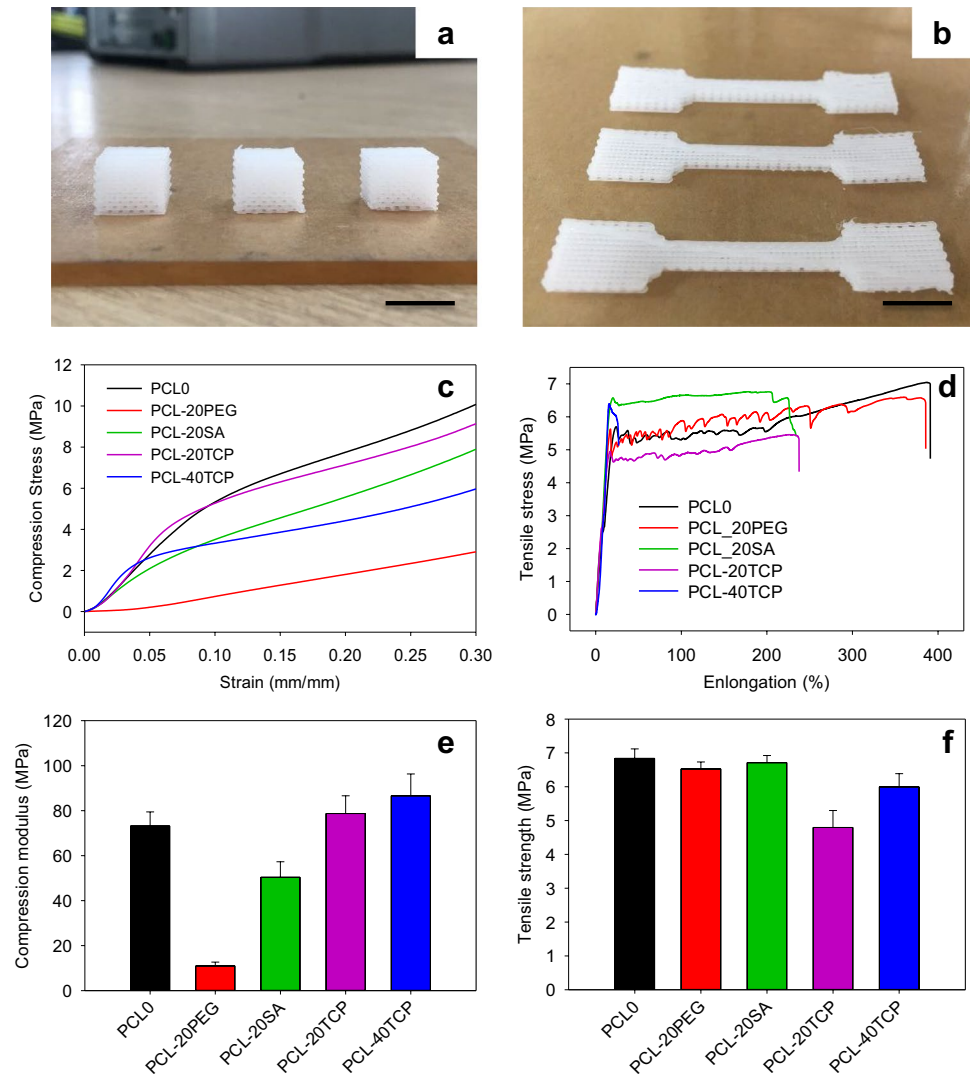
It also noted that the tensile strength of the composite scaffold was reduced upon incorporating TCP ceramic phase into the PCL scaffold. As a result, the PCL-TCP exhibited lower tensile strength than the PCL. The poor tensile strength of the TCP ceramic phase is due to intrinsic brittleness. However, the PCL-40TCP has higher tensile strength when compared to the PCL-20TCP. This can be explained by the stress–strain behaviors of the PCL-40TCP. Since the PCL-40TCP exhibits the typical stress–strain behavior of the ceramic phase, the

polymer could potentially enhance the material toughness, thereby increasing the tensile strength of the PCL-40TCP.

#### f) Cell attachment

The cell attachment and proliferation onto the scaffolds were conducted by utilizing FDA staining after 3 days of cell culture. Figure 13 illustrates the live human lung fibroblast cells stained with a green dye. As observed, the cells adhered to all PCL-based scaffolds. The PCL0 scaffold exhibited the lowest cell density on its surface possibly due to its hydrophobic nature and low surface roughness that made it less favorable for cell adhesion. In contrast, the addition of fillers to pure PCL to increase the hydrophilicity and surface roughness significantly enhanced cell adhesion on the composite scaffold surfaces. Particularly, the PCL-20SA

**Fig. 12** Mechanical property comparison of PCL-based composite specimens: compression test specimens (a); tensile test specimens (b); compression stress and strain curves (c); tensile stress and strain curves (d); compression modulus (e); and tensile strength (f) for PCL-based scaffolds. Scale bar 10 mm



scaffold demonstrated a significantly higher density of live cells compared to other PCL-based composite scaffolds, indicating that the inclusion of SA greatly promoted cell proliferation (Fig. 13c). Additionally, the cell density on the surface of the PCL-20PEG scaffold was slightly higher than that of the PCL-TCP based scaffold. Increasing the TCP content from 20 to 40 wt% did not yield a significant difference in the observed cell adhesion. In general, the combination of PCL with other materials exhibited improved biocompatibility, which facilitated cell attachment and proliferation.

### 4.3 The effects of printing parameters on printed line width

#### a) Pure PCL

Figure 14 presents the statistical distribution of the SLW influenced by printing parameters, namely, printing

temperature (T), extrusion speed (E), and printing speed (F), in consideration of a targeted printing line width of 0.4 mm. Concerning the printing temperature, it can be observed that there is a significant increase in the average SLW as the printing temperature rises from 90 to 100 °C. Simultaneously, a slight increase in SLW is observed when the printing temperature increases from 100 to 110 °C. Concerning the printing speed, the SLW mostly decreases with increased printing speeds. Remarkably, at a printing speed of 5 mm/s, the SLW tends to exceed the expected line width of 0.4 mm in most cases due to the larger extruded material at a lower printing speed. Specifically, at a printing temperature of 90 °C (Fig. 14a–c), a slight decrease in SLW is noted as printing speed increases from 6 to 9 mm/s, as compared to those with a printing temperature of 100 °C (Fig. 14d–f) and 110 °C (Fig. 14g–i). In addition, a minimal change in SLW is observed at E = 11 rpm and T = 90 °C across different printing speed values (Fig. 14a). The effect of varying extrusion speeds on the SLW has been slightly observed across

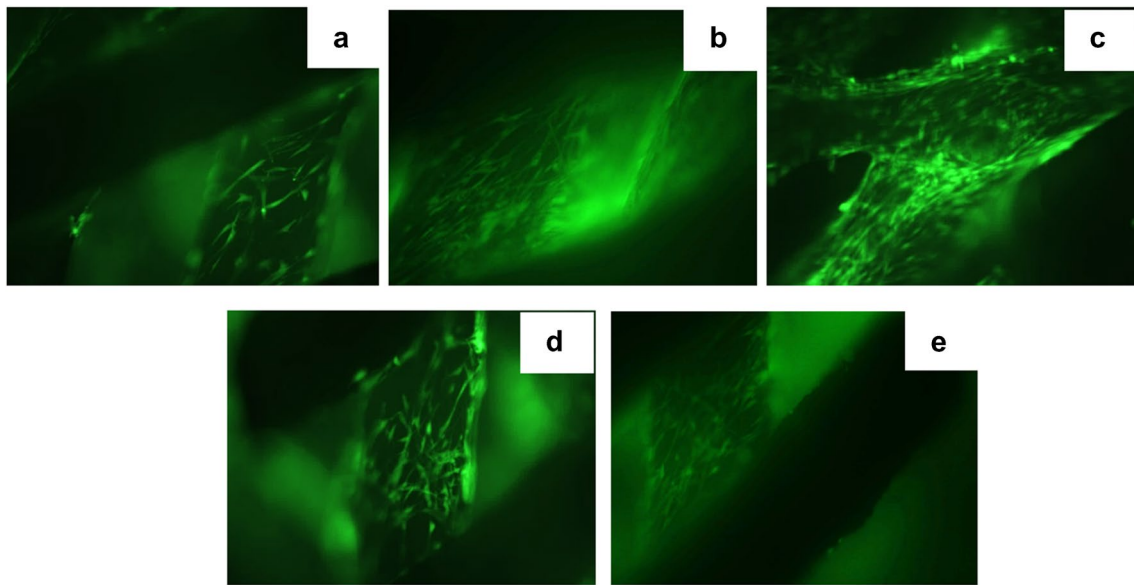


**Fig. 13** Comparison of cell adhesion on different PCL-based scaffold surfaces after 3-day cell culture: **a** PCL0; **b** PCL-20PEG; **c** PCL-20SA; **d** PCL-20TCP, and **e** PCL-40TCP. Green fluorescence indicates live cells

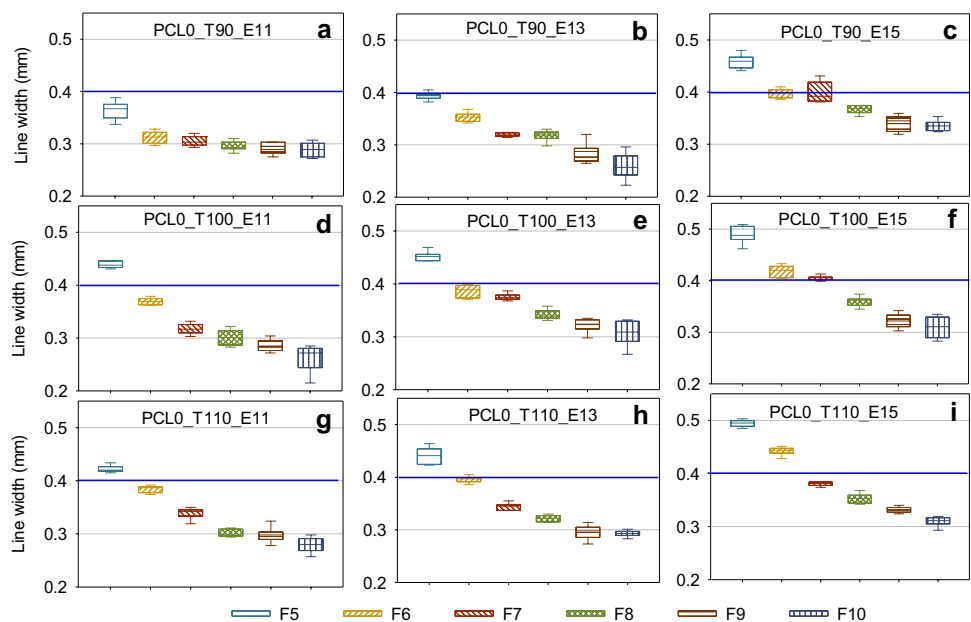
all printing tests. Therefore, the slight change in extrusion speed would not affect the printing quality of the scaffold. In other stated, the control of the printed line is not significantly affected by extrusion speed.

Regarding the stability of the SLW, it can be observed that the SLW exhibited higher dimensional accuracy at elevated printing temperatures. This can be attributed to the consistent extrusion flow of molten PCL at higher temperatures (Fig. 14h,i). However, during printing tests at 110 °C, over-extrusion was more prevalent after pausing the extrusion than at lower temperatures. When the SLW is less than the

print layer thickness (0.35 mm), the printed line width may exhibit instability due to inadequate adhesion to the previous layer, leading to SLW with higher tolerance (Fig. 14b,e). To accelerate the drying process of each printed layer, it is imperative to maintain the ambient temperature at 25 °C and employs a cooling fan directed toward the printed layer.

The distribution in Fig. 15 indicates the average SLW exhibited a similar fluctuations’ trend across different printing conditions, characterized by both an upward and a downward trend. When printing speeds were set at 8 mm/s or 9 mm/s, there was minimal variation in the average SLW

**Fig. 14** Effects of printing parameters on printed line width for PCL0 material at printing temperature 90 °C and extrusion speed 11, 13, and 15 rpm respectively (**a,b,c**); printing temperature 100 °C and extrusion speed 11, 13, and 15 rpm respectively (**d,e,f**); and printing temperature 110 °C and extrusion speed 11, 13, and 15 rpm respectively (**g,h,i**). The blue line shows the target line width of 0.4 mm



across various printing temperatures and extrusion speed. Notably, at an extrusion speed of 15 rpm and a printing speed of 7 mm/s (E15\_F7), the average SLW value closely approached the target line width of 0.4 mm compared to other printing conditions regardless of the tested printing temperature. The results indicated that the SLW is notably impacted by the printing speed *F* compared to other printing parameters (*E* and *T*). By carefully selecting appropriate printing parameters, a wide range of desired dimensions for the printed line width, ranging from 300 to 500  $\mu\text{m}$ , can be achieved.

## b) PCL-based composites

Three different types of additive materials, namely, a synthetic polymer (PEG), a natural polymer (SA), and a ceramic (TCP), were incorporated into the base material (PCL) at a content of 20 wt%. Specifically, the printability of the DPSE printer head was evaluated using the TCP additive, which consisted of ceramic powder at 40 wt%. The effects of printing parameters on SLW for the PCL-20PEG, PCL-20SA, and PCL-TCP (20% TCP and 40% TCP) formulations are depicted in Fig. 16 and Fig. 17, respectively.

To achieve the equivalent SLW to that of printing with PCL0, it is necessary to considerably decrease the printing speed to 4 mm/s, accompanied by a higher extrusion speed ( $E = 17$  rpm) for the PCL-20PEG material, as illustrated in Fig. 16b. At the extrusion speed of 15 rpm (Fig. 16a), it has been observed that none of printing are formed at a printing speed greater than 5 mm/s. The attainment of the desired SLW is contingent upon the extrusion speed being increased

to 17 rpm. This behavior can be attributed to the waxy properties of the PEG material, which increases the friction during material transfer, impeding the extrusion flow within the barrel. Furthermore, the PCL-20PEG material demonstrated high sensitivity to variations in printing temperatures, making it challenging to determine the appropriate printing temperature for the PCL-20PEG mixture. Therefore, the SLW exhibited a low dimensional accuracy, particularly due to the non-uniform mixture of two materials. The SLW of PCL-20SA is significantly higher compared to the SLW of PCL0 under the same *T* and *E* printing conditions, as shown in Fig. 16c–d. This phenomenon can be attributed to the swelling behavior of the hydrogel material upon extrusion from the nozzle.

The PCL-20TCP exhibited the highest printability to other mixtures, with small dimensional tolerance, as depicted in Fig. 17 a and b. It can be explained by the rapid drying of the printed line that it contributes to establishing a stable printed line. The PCL-20TCP powder mixture exhibited an extended range of printing speeds. By adjusting the printing speed from 5 to 10 mm/s at  $T_{90}$  and  $E_{13}$ , the average line width (SLW) decreased from 0.62 to 0.4 mm (Fig. 17b). The experimental finding indicated a positive correlation between the printing temperature and the average SLW, as shown in Fig. 17 b and c. This flexibility allows users to select appropriated printing parameters to achieve their desired line width. Furthermore, significant changes in the printing characteristics were observed when the TCP composition in the mixture was increased from 20 to 40 wt%. Under the same printing parameters, the SLW of PCL-40TCP was significantly lower compared to that of PCL-20TCP, as shown in Fig. 17d and e when the printing speed was between 5 and 7 mm/s. This can be attributed to the higher proportion of ceramic powders, which can impede the flow of the melted composite from the printhead, particularly when printing speeds are lower. Flow clogging was observed during the printing process when the extrusion speed exceeded 10 rpm, resulting in the slipping of the extruding step motor. Therefore, to prevent the clogging phenomenon during the printing of the PCL-40TCP composite, it is recommended to adjust the extrusion speed to be less than 10 rpm and greater than 8 rpm (Fig. 17e,f).

Figure 18 illustrates the distribution of SLW around the target dimension of 0.4 mm (indicated by the blue solid line) by taking measurement of SWL at various location for different PCL-based composite printing samples using the recommended printing parameters from above experiments. The PCL0 specimens exhibited an average SLW of  $395.9 \pm 5.8 \mu\text{m}$ , indicating a high level of quality printing accuracy, while the PCL-20PEG specimens displayed a higher deviation in SLW ( $418.1 \pm 21.1 \mu\text{m}$ ) due to the significant difference in the melting point temperatures between PCL and PEG materials. This discrepancy led

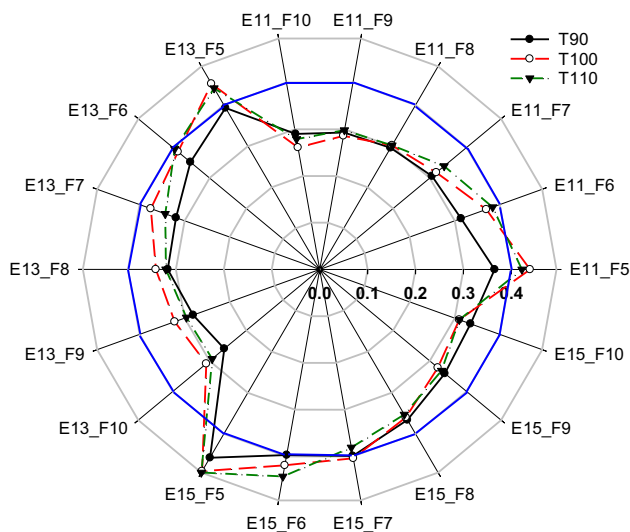


**Fig. 15** Average printed line width distribution around the desired SLW (blue line represented for the targeted printing line width of 0.4 mm) for PCL0 material with the same *E* and *F* at three different *T* 90 °C, 100 °C, and 110 °C



**Fig. 16** Effects of printing parameters on printed line width at printing temperature 90 °C for PCL-20PEG with extrusion speed 15 rpm and 17 rpm, respectively (a,b) and PCL-20SA at printing temperature with extrusion speed 10 rpm and 13 rpm, respectively (c,d)

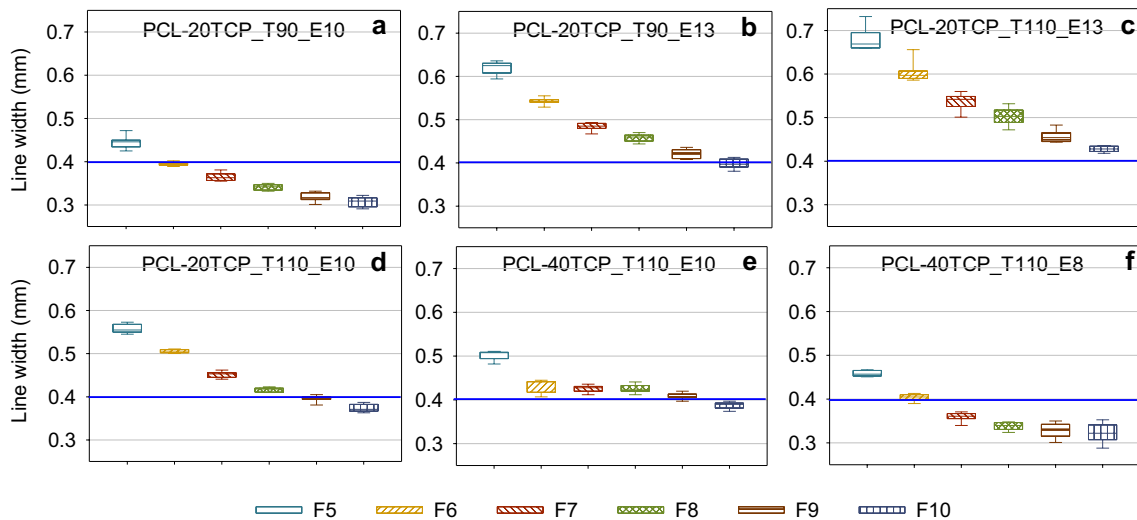
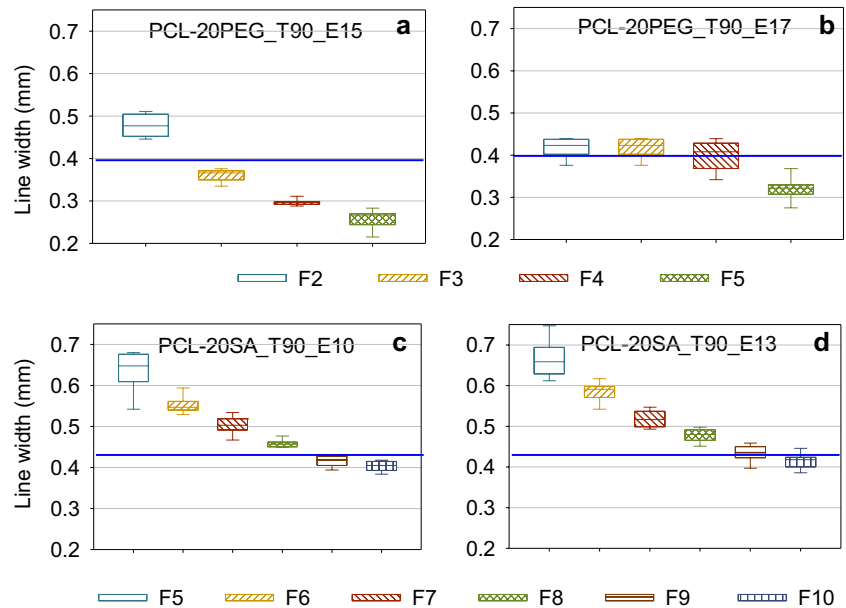


**Fig. 17** Effects of printing parameter on printed line width for PCL-20TCP at T=90 °C and E=10 rpm and 13 rpm respectively (a,b); at T=110 °C and E=13 rpm and 10 rpm respectively (c,d); and for PCL-40TCP, at T=110 °C and E=10 and 8 rpm respectively (e,f)

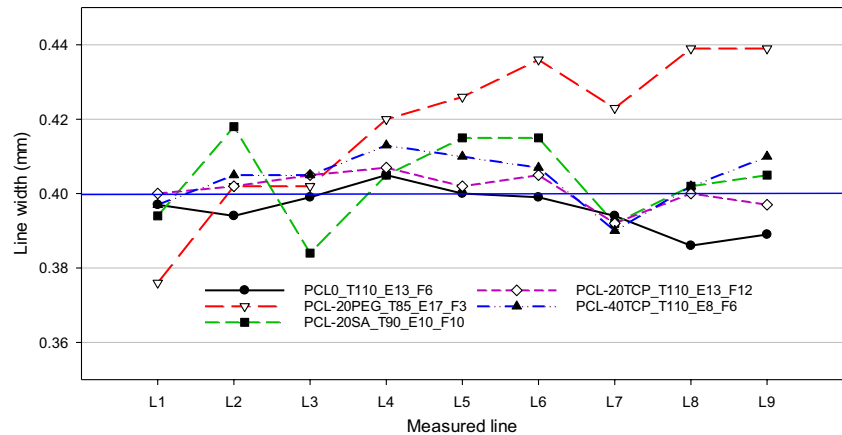
to instability in the molten region, affecting the overall material state. Furthermore, the nonuniform mixing of two materials with different melting points and viscosity properties also exerts a substantial influence on the variation in the printed line width.

The PCL-20SA specimen displayed diminished printing accuracy, as indicated by an average SLW of  $403.3 \pm 11.6 \mu\text{m}$ . This decrease can be primarily attributed to the observed swell phenomena during the printing process of SA powder. At an SA content of 20 wt%, the PCL component constitutes a significant proportion of the composite material, influencing the presence or absence of SA particles along the printed line. The swelling and

clustering of SA powder contributed by the enlargement of line sizes, particularly noticeable at specific locations such as L2 and L6. Conversely, positions with a lower quantity of SA powder (L3 and L7) exhibited comparatively smaller line sizes. Consequently, the variation in line sizes becomes remarkably significant, emphasizing the impact of these factors on printing accuracy.

The PCL-20TCP material demonstrated the most stable SLW, with an average SLW of  $401.1 \pm 4.6 \mu\text{m}$ . This can be attributed to the immediate drying of the printed line upon deposition from the nozzle for PCL-TCP composites, providing strong support for the subsequent layer. However, at higher concentrations of ceramic powders in the composite

**Fig. 18** Printed line width distribution at different measured positions around the desired line width of 0.4 mm, as indicated by the solid blue line



(PCL-40TCP), the accumulation of ceramic powder and subsequent nozzle clogging resulted in slightly lower printing accuracy, with an average SLW of  $404.3 \pm 7.2 \mu\text{m}$ . The differences between the SLW and the designed line width can be attributed to the varying effects of various additives and material compositions on the uniformity of the material state. In general, the achieved printing accuracy of PCL0, PCL-20TCP, and PCL-40TCP with the DPSE printer head in this work is equivalent to that of an HB design-based printer head [35, 36].

## 5 Conclusions

The study presented a newly developed DPSE printer head and investigates the fabrication and characteristics of PCL-based composite scaffolds. This work demonstrated the high potential application of the DPSE printer head in producing 3D interconnected and porous PCL-based composite scaffolds for application in tissue engineering. The following conclusions could be drawn from this work:

- Both numerical modeling analysis and experimental results demonstrated that modifications in the HE designs, such as the introduction of a Teflon screw, Teflon top barrel, and O-rings, have effectively mitigated polymer clogging during extrusion by reducing the immediate temperature inside the barrel.
- The DPSE printer head exhibited favorable attributes, including a simple structure, low production cost, improved material consumption efficiency, and reasonable printing accuracy. These characteristics make it a promising printer head not only for pure PCL but also for PCL-based composite scaffolds containing various types and compositions of additive materials.
- The PCL-20TCP composite reached the highest-level printing accuracy, with an accuracy of 2%, while the PCL-20PEG composite showed the lowest accuracy

of 10%. The addition of PEG and SA to PCL material significantly reduced the water contact angle compared to TCP. Among the PCL-based composite scaffolds, it was observed that the PCL-40TCP scaffold exhibited the highest compression modulus, while the PCL-20SA specimen demonstrated the highest tensile strength. Moreover, the PCL-20SA scaffold exhibited the highest cell density adhesion to the surface after 3-day seeding.

- Future research will focus on investigating cell proliferation and bioactivity with PCL-based composite scaffolds.

**Author contribution** Trung Kien Nguyen and Lan Xuan Phung developed the printer head, investigated the printability, and fabricated the scaffolds. Van-Sang Pham performed the numerical modeling thermal analysis. Bang Thi Le and Truong Do carried out and evaluated the scaffold characteristics. Minh Hong Thi Nguyen performed the cell seeding experiment on the scaffolds. Phuong Tran evaluated the methodology. Lan Xuan Phung created the research direction, reviewed the related work, and supervised the project. Each author is in charge of writing their part of the manuscript. All authors discussed the results and contributed to the final manuscript.

**Funding** This research is funded by the Vingroup Innovation Foundation (VINIF) through the project VINIF.2020.DA13.

## Declarations

**Competing interests** The authors declare no competing interests.

## References

1. Gleadall A, Visscher D, Yang J, Thomas D, Segal J (2018) Review of additive manufactured tissue engineering scaffolds: relationship between geometry and performance. *Burns & Trauma* 6:1–16. <https://doi.org/10.1186/s41038-018-0121-4>

2. Nikolova MP, Chavali MS (2019) Recent advances in biomaterials for 3D scaffolds: a review. *Bioact Mater* 4:271–292. <https://doi.org/10.1016/j.bioactmat.2019.10.005>
3. Loh QL, Choong C (2013) Three-dimensional scaffolds for tissue engineering applications: role of porosity and pore size. *Tissue Eng Part B Rev* 19(6):485. <https://doi.org/10.1089/TEN.TEB.2012.0437>
4. Guo A, Wang J, Tang R, Kong H, Kong D, Qu P, Wang S, Wang H, Hu Y (2023) Insights into the effects of epoxy resin infiltration on powder aging issue induced by powder recycling in powder bed fusion of Nylon12 materials. *J Mater Res Technol* 23:3151–3165. <https://doi.org/10.1016/j.jmrt.2023.02.003>
5. Han J, Wu J, Xiang X, Xie L, Chen R, Li L, Ma K, Sun Q, Yang R, Huang T, Tong L, Zhu L, Wang H, Wen C, Zhao Y, Wang J (2023) Biodegradable BBG/PCL composite scaffolds fabricated by selective laser sintering for directed regeneration of critical-sized bone defects. *Mater Des* 225:111543. <https://doi.org/10.1016/j.matdes.2022.111543>
6. Guo A, Kong D, Zhou X, Kong H, Qu P, Wang S, Wang H, Hu Y (2022) Method for preparing damage-resistant 3D-printed ceramics via interior-to-exterior strengthening and toughening. *Addit Manuf* 60:103272. <https://doi.org/10.1016/j.addma.2022.103272>
7. Pugliese R, Graziosi S (2023) Biomimetic scaffolds using triply periodic minimal surface-based porous structures for biomedical applications. *SLAS Technol* 28(3):165–182. <https://doi.org/10.1016/j.slast.2023.04.004>
8. Rajan K, Samykano M, Kadirgama K, Harun WSW, Rahman MM (2022) Fused deposition modeling: process, materials, parameters, properties, and applications. *Int J Adv Manuf Technol* 120(3–4):1531–1570. <https://doi.org/10.1007/s00170-022-08860-7>
9. Winarso R, Anggoro PW, Ismail R, Jamari J, Bayuseno AP (2022) Application of fused deposition modeling (FDM) on bone scaffold manufacturing process: a review. *Heliyon* 8(11):e11701. <https://doi.org/10.1016/j.heliyon.2022.e11701>
10. Melcova V, Svoradova K, Mencik P, Kontarova S, Rampichova M, Hedvicakova V, Sovkova V, Prikryl R, Vojtova L (2020) FDM 3D Printed composites for bone tissue engineering based on plasticized poly(3-hydroxybutyrate)/poly(d, l-lactide) blends. *Polymers (Basel)* 12(12):2806. <https://doi.org/10.3390/polym12122806>
11. Bruyas A, Lou F, Stahl AM, Gardner M, Maloney W, Goodman S, Yang YP (2018) Systematic characterization of 3D-printed PCL/beta-TCP scaffolds for biomedical devices and bone tissue engineering: influence of composition and porosity. *J Mater Res* 33(14):1948–1959. <https://doi.org/10.1557/jmr.2018.112>
12. Siddiqui N, Asawa S, Birru B, Baadhe R, Rao S (2018) PCL-based composite scaffold matrices for tissue engineering applications. *Mol Biotechnol* 60(7):506–32. <https://doi.org/10.1007/S12033-018-0084-5>
13. Kutikov AB, Song J (2015) Biodegradable PEG-based amphiphilic block copolymers for tissue engineering applications. *ACS Biomater Sci Eng* 1(7):463–480. <https://doi.org/10.1021/acsbomaterials.5b00122>
14. Park SA, Lee SJ, Seok JM, Lee JH, Kim WD, Kwon IK (2018) Fabrication of 3D printed PCL/PEG polyblend scaffold using rapid prototyping system for bone tissue engineering application. *J Bionic Eng* 15(3):435–42. <https://doi.org/10.1007/S42235-018-0034-8>
15. Cao C, Huang P, Prasopthum A, Parsons AJ, Ai F, Yang J (2021) Characterisation of bone regeneration in 3D printed ductile PCL/PEG/hydroxyapatite scaffolds with high ceramic micro-particle concentrations. *Biomater Sci* 10(1):138–152. <https://doi.org/10.1039/d1bm01645h>
16. Bagde AD, Kuthe AM, Quazi S, Gupta V, Jaiswal S, Jyothilal S, Lande N, Nagdeve S (2019) State of the art technology for bone tissue engineering and drug delivery. *Irbm* 40(3):133–144. <https://doi.org/10.1016/j.irbm.2019.03.001>
17. Freeman FE, Kelly DJ (2017) Tuning alginate bioink stiffness and composition for controlled growth factor delivery and to spatially direct MSC fate within bioprinted tissues. *Sci Rep* 7(1):17042. <https://doi.org/10.1038/s41598-017-17286-1>
18. Kim Y, Kim G (2013) Collagen/alginate scaffolds comprising core (PCL)-shell (collagen/alginate) struts for hard tissue regeneration: fabrication, characterisation, and cellular activities. *J Mater Chem B* 1(25):3185–3194. <https://doi.org/10.1039/c3tb20485e>
19. Kim YB, Kim GH (2015) PCL/alginate composite scaffolds for hard tissue engineering: fabrication, characterization, and cellular activities. *ACS Comb Sci* 17(2):87–99. <https://doi.org/10.1021/co500033h>
20. Norouzi MR, Ghasemi-Mobarakeh L, Itef F, Schoeller J, Fashandi H, Borzi A, Neels A, Fortunato G, Rossi RM (2022) Emulsion electrospinning of sodium alginate/poly(epsilon-caprolactone) core/shell nanofibers for biomedical applications. *Nanoscale Adv* 4(13):2929–2941. <https://doi.org/10.1039/d2na00201a>
21. Yao Z, Qian Y, Jin Y, Wang S, Li J, Yuan WE, Fan C (2022) Biomimetic multilayer polycaprolactone/sodium alginate hydrogel scaffolds loaded with melatonin facilitate tendon regeneration. *Carbohydr Polym* 277:118865. <https://doi.org/10.1016/j.carbpol.2021.118865>
22. Dwivedi R, Kumar S, Pandey R, Mahajan A, Nandana D, Katti DS, Mehrotra D (2020) Polycaprolactone as biomaterial for bone scaffolds: review of literature. *J Oral Biol Craniofac Res* 10(1):381–388. <https://doi.org/10.1016/j.jobcr.2019.10.003>
23. Heo SJ, Kim SE, Wei J, Hyun YT, Yun HS, Kim DH, Shin JW, Shin JW (2009) Fabrication and characterization of novel nano- and micro-HA/PCL composite scaffolds using a modified rapid prototyping process. *J Biomed Mater Res A* 89(1):108–116. <https://doi.org/10.1002/jbm.a.31726>
24. Aydogdu MO, Mutlu B, Kurt M, Inan AT, Kuruca SE, Erdemir G, Sahin YM, Ekren N, Oktar FN, Gunduz O (2019) Developments of 3D polycaprolactone/beta-tricalcium phosphate/collagen scaffolds for hard tissue engineering. *J Aust Ceram* 55(3):849–55. <https://doi.org/10.1007/S41779-018-00299-Y>
25. Li Y, Yu Z, Ai F, Wu C, Zhou K, Cao C, Li W (2021) Characterization and evaluation of polycaprolactone/hydroxyapatite composite scaffolds with extra surface morphology by cryogenic printing for bone tissue engineering. *Mater Des* 205:109712. <https://doi.org/10.1016/j.matdes.2021.109712>
26. Albrecht LD, Sawyer SW, Soman P (2016) Developing 3D scaffolds in the field of tissue engineering to treat complex bone defects. *3D Print Addit Manuf* 3(2):106–12. <https://doi.org/10.1089/3DP.2016.0006>
27. Beatrice CAG, Shimomura KMB, Backes EH, Harb SV, Costa LC, Passador FR, Pessan LA (2021) Engineering printable composites of poly (epsilon-polycaprolactone) / beta-tricalcium phosphate for biomedical applications. *Polym Compos* 42(3):1198–1213. <https://doi.org/10.1002/pc.25893>
28. Luo W, Zhang S, Lan Y, Huang C, Wang C, Lai X, Chen H, Ao N (2018) 3D printed porous polycaprolactone/oyster shell powder (PCL/OSP) scaffolds for bone tissue engineering. *Mater Res Express* 5(4):045403. <https://doi.org/10.1088/2053-1591/AAB916>
29. Boyle BM, Xiong PT, Mensch TE, Werder TJ, Miyake GM (2019) 3D printing using powder melt extrusion. *Addit Manuf* 29:100811. <https://doi.org/10.1016/j.addma.2019.100811>
30. Liu H, Ahlinder A, Yassin MA, Finne-Wistrand A, Gasser TC (2020) Computational and experimental characterization of 3D-printed PCL structures toward the design of soft biological

- tissue scaffolds. *Mater Des* 188:108488. <https://doi.org/10.1016/J.MATDES.2020.108488>
31. Kim JY, Lee TJ, Cho DW, Kim BS (2010) Solid free-form fabrication-based PCL/HA scaffolds fabricated with a multi-head deposition system for bone tissue engineering. *J Biomater Sci Polym Ed* 21(6–7):951–962. <https://doi.org/10.1163/156856209X458380>
  32. Andrea Roberto C, Sinha R, Harings J, Bernaerts KV, Mota C, Moroni L (2021) Additive manufacturing using melt extruded thermoplastics for tissue engineering. *Methods Mol Biol* 2147(2147):75–99. [https://doi.org/10.1007/978-1-0716-0611-7\\_7](https://doi.org/10.1007/978-1-0716-0611-7_7)
  33. Domingos M, Chiellini F, Gloria A, Ambrosio L, Bartolo P, Chiellini E (2012) Effect of process parameters on the morphological and mechanical properties of 3D Bioextruded poly( $\epsilon$ -caprolactone) scaffolds. *Rapid Prototyp J* 18(1):56–67. <https://doi.org/10.1108/13552541211193502>
  34. Liu F, Vyas C, Poologasundarampillai G, Pape I, Hinduja S, Mirihanage W, Bartolo P (2018) Structural evolution of PCL during melt extrusion 3D printing. *Macromol Mater Eng* 303(2):1700494. <https://doi.org/10.1002/MAME.201700494>
  35. Huang B, Vyas C, Roberts I, Poutrel QA, Chiang WH, Blaker JJ, Huang Z (2018) Bártolo P (2019) Fabrication and characterisation of 3D printed MWCNT composite porous scaffolds for bone regeneration. *Mater Sci Eng, C* 98:266–278. <https://doi.org/10.1016/j.msec.2018.12.100>
  36. Hou Y, Wang W, Bártolo P (2020) Novel poly( $\epsilon$ -caprolactone)/graphene scaffolds for bone cancer treatment and bone regeneration. *3D Printing and Additive Manufacturing* 7(5):222–229. <https://doi.org/10.1089/3DP.2020.0051>
  37. Wang F, Shor L, Darling A, Khalil S, Sun W, Güçeri S, Lau A (2004) Precision extruding deposition and characterization of cellular poly- $\epsilon$ -caprolactone tissue scaffolds. *Rapid Prototyp J* 10(1):42–49. <https://doi.org/10.1108/13552540410512525>
  38. Marchewka J, Laska J (2020) Processing of poly-L-lactide and poly(L-lactide-co-trimethylene carbonate) blends by fused filament fabrication and fused granulate fabrication using RepRap 3D printer. *Int J Adv Manuf Technol* 106(11–12):4933–4944. <https://doi.org/10.1007/s00170-020-04981-z>
  39. Dávila JL, Freitas MS, Inforçatti Neto P, Silveira ZC, Silva JVL, D'Ávila MA (2016) Fabrication of PCL/ $\beta$ -TCP scaffolds by 3D mini-screw extrusion printing. *J Appl Polym Sci* 133(15):1–9. <https://doi.org/10.1002/app.43031>
  40. Whyman S, Arif KM, Potgieter J (2018) Design and development of an extrusion system for 3D printing biopolymer pellets. *Int J Adv Manuf Technol* 96(9–12):3417–3428. <https://doi.org/10.1007/s00170-018-1843-y>
  41. Reyes RL, Ghim M-S, Kang N-U, Park J-W, Gwak S-J, Cho Y-S (2022) Development and assessment of modified-honeycomb-structure scaffold for bone tissue engineering. *Addit Manuf* 54:102740. <https://doi.org/10.1016/j.addma.2022.102740>
  42. Feuerbach T, Thommes M (2021) Design and characterization of a screw extrusion hot-end for fused deposition modeling. *Molecules*. 26(3):590. <https://doi.org/10.3390/molecules26030590>
  43. Tian J, Zhang R, Wu Y, Xue P (2021) Additive manufacturing of wood flour/polyhydroxyalkanoates (PHA) fully bio-based composites based on micro-screw extrusion system. *Mater Des*. 199:109418. <https://doi.org/10.1016/j.matdes.2020.109418>
  44. Kang N-U, Hong MW, Kim YY, Cho Y-S, Lee S-J (2019) Development of a powder extruder system for dual-pore tissue-engineering scaffold fabrication. *J Bionic Eng* 16(4):686–695. <https://doi.org/10.1007/s42235-019-0055-y>
  45. Samiula BKA, Saitoa A, Khoslaa A, Kawakamia M, Furukawa H (2009) Development of multi-material 3D printer. *ECS Transactions* 88(1):449–53
  46. Jeon H, Lee H, Kim G (2014) A surface-modified poly( $\epsilon$ -caprolactone) scaffold comprising variable nanosized surface-roughness using a plasma treatment. *Tissue Eng Part C Methods* 20(12):951–963. <https://doi.org/10.1089/ten.tec.2013.0701>
  47. Han J, Li Z, Sun Y, Cheng F, Zhu L, Zhang Y, Zhang Z, Wu J, Wang J (2022) Surface roughness and biocompatibility of polycaprolactone bone scaffolds: an energy-density-guided parameter optimization for selective laser sintering. *Front Bioeng Biotechnol* 10:888267. <https://doi.org/10.3389/fbioe.2022.888267>
  48. Kim CH, Khil MS, Kim HY, Lee HU, Jahng KY (2006) An improved hydrophilicity via electrospinning for enhanced cell attachment and proliferation. *J Biomed Mater Res B Appl Biomater* 78(2):283–290. <https://doi.org/10.1002/jbm.b.30484>
  49. Ehtesabi H, Massah F (2021) Improvement of hydrophilicity and cell attachment of polycaprolactone scaffolds using green synthesized carbon dots. *Mater Today Sustain* 13:100075. <https://doi.org/10.1016/j.mtsust.2021.100075>
  50. Yedekçi B, Tezcaner A, Yılmaz B, Demir T, Evis Z (2022) 3D porous PCL-PEG-PCL / strontium, magnesium and boron multi-doped hydroxyapatite composite scaffolds for bone tissue engineering. *J Mech Behav Biomed Mater* 125:104941. <https://doi.org/10.1016/j.jmbbm.2021.104941>
  51. Chen J, Wu A, Yang M, Ge Y, Pristijono P, Li J, Xu B, Mi H (2021) Characterization of sodium alginate-based films incorporated with thymol for fresh-cut apple packaging. *Food Control* 126:108063. <https://doi.org/10.1016/j.foodcont.2021.108063>
  52. Badita CRAD, Burducea C, Mereuță P (2020) Characterization of sodium alginate based films. *Romanian J Phys* 65:1–8
  53. Ishikawa K (2010) Bone substitute fabrication based on dissolution-precipitation reactions. *Materials (Basel)* 3(2):1138–1155. <https://doi.org/10.3390/ma3021138>
  54. Ślósarczyk A, Paszkiewicz Z, Paluszkiwicz C (2005) FTIR and XRD evaluation of carbonated hydroxyapatite powders synthesized by wet methods. *J Mol Struct* 744–747:657–661. <https://doi.org/10.1016/j.molstruc.2004.11.078>
  55. Goonoo N, Bhaw-Luximon A, Bowlin GL, Jhurry D (2013) An assessment of biopolymer- and synthetic polymer-based scaffolds for bone and vascular tissue engineering. *Polym Int* 62(4):523–533. <https://doi.org/10.1002/pi.4474>
  56. Zhang S, Vijayavenkataraman S, Lu WF, Fuh JYH (2019) A review on the use of computational methods to characterize, design, and optimize tissue engineering scaffolds, with a potential in 3D printing fabrication. *J Biomed Mater Res B Appl Biomater* 107(5):1329–1351. <https://doi.org/10.1002/jbm.b.34226>
  57. Vozniak I, Hosseinnezhad R, Morawiec J, Galeski A (2020) Microstructural evolution of poly( $\epsilon$ -caprolactone), its immiscible blend, and in situ generated nanocomposites. *Polymers* 12(11):2587. <https://doi.org/10.3390/polym12112587>

**Publisher's note** Springer Nature remains neutral with regard to jurisdictional claims in published maps and institutional affiliations.

Springer Nature or its licensor (e.g. a society or other partner) holds exclusive rights to this article under a publishing agreement with the author(s) or other rightsholder(s); author self-archiving of the accepted manuscript version of this article is solely governed by the terms of such publishing agreement and applicable law.